OPEN ACCESS
CellPress

Cell Reports
Article

Dysregulated Expression of Neuregulin-1 by Cortical Pyramidal Neurons Disrupts Synaptic Plasticity

Amit Agarwal,[1,7,8] Mingyue Zhang,[2,8] Irina Trembak-Duff,[2,8] Tilmann Unterbarnscheidt,[1,8] Konstantin Radyushkin,[3,9] Payam Dibaj,[1] Daniel Martins de Souza,[4,10] Susann Boretius,[5] Magdalena M. Brzózka,[1,11] Heinz Steffens,[6] Sebastian Berning,[6] Zenghui Teng,[2] Maike N. Gummert,[1] Martesa Tantra,[3] Peter C. Guest,[4] Katrin I. Willig,[6] Jens Frahm,[5] Stefan W. Hell,[6] Sabine Bahn,[4] Moritz J. Rossner,[1,11] Klaus-Armin Nave,[1] Hannelore Ehrenreich,[3] Weiqi Zhang,[2,*] and Markus H. Schwab[1,12,*]

[1]Department of Neurogenetics, Max Planck Institute of Experimental Medicine, 37075 Göttingen, Germany
[2]Laboratory of Molecular Psychiatry, Department of Psychiatry, University of Münster, 48149 Muenster Germany
[3]Clinical Neuroscience, Max Planck Institute of Experimental Medicine, 37075 Göttingen, Germany
[4]Institute of Biotechnology, University of Cambridge, Cambridge CB2 1QT, UK
[5]Biomedizinische NMR Forschungs GmbH, Max Planck Institute of Biophysical Chemistry, 37077 Göttingen, Germany
[6]Department of NanoBiophotonics, Max Planck Institute for Biophysical Chemistry, 37077 Göttingen, Germany
[7]Solomon H. Snyder Department of Neuroscience, Johns Hopkins University, Baltimore, MD 21025, USA
[8]Co-first author
[9]Present address: Department of Physiological Chemistry, Focus Program Translational Neurosciences, Johannes Gutenberg University of Mainz, 55131 Mainz, Germany
[10]Present address: Laboratory of Neuroproteomics, Department of Biochemistry, Institute of Biology, State University of Campinas (UNICAMP), Campinas, Sao Paulo 13083-970, Brazil
[11]Present address: Department of Psychiatry, Ludwig-Maximilian-University Munich, 81377 Munich, Germany
[12]Present address: Cellular Neurophysiology, Hannover Medical School, 30625 Hannover, Germany
*Correspondence: wzhang@uni-muenster.de (W.Z.), schwab@em.mpg.de (M.H.S.)
http://dx.doi.org/10.1016/j.celrep.2014.07.026

SUMMARY

Neuregulin-1 (*NRG1*) gene variants are associated with increased genetic risk for schizophrenia. It is unclear whether risk haplotypes cause elevated or decreased expression of NRG1 in the brains of schizophrenia patients, given that both findings have been reported from autopsy studies. To study NRG1 functions in vivo, we generated mouse mutants with reduced and elevated NRG1 levels and analyzed the impact on cortical functions. Loss of NRG1 from cortical projection neurons resulted in increased inhibitory neurotransmission, reduced synaptic plasticity, and hypoactivity. Neuronal overexpression of cysteine-rich domain (CRD)-NRG1, the major brain isoform, caused unbalanced excitatory-inhibitory neurotransmission, reduced synaptic plasticity, abnormal spine growth, altered steady-state levels of synaptic plasticity-related proteins, and impaired sensorimotor gating. We conclude that an "optimal" level of NRG1 signaling balances excitatory and inhibitory neurotransmission in the cortex. Our data provide a potential pathomechanism for impaired synaptic plasticity and suggest that human NRG1 risk haplotypes exert a gain-of-function effect.

INTRODUCTION

Neuregulin-1 (NRG1) is a pleiotropic growth and differentiation factor, which signals to receptor tyrosine kinases of the ErbB family (Falls, 2003). The human *NRG1* gene is a major schizophrenia susceptibility gene (Ayalew et al., 2012; Li et al., 2006), but the underlying link to pathophysiology is not known. Virtually all "at-risk" haplotypes map to noncoding regions of the human *NRG1* gene (Stefansson et al., 2002; Weickert et al., 2012), suggesting that altered NRG1 expression increases disease susceptibility. Indeed, both reduced and increased expression of distinct NRG1 variants have been observed in studies of postmortem brain tissue from schizophrenia patients (Bertram et al., 2007; Law et al., 2006). This includes elevated expression of membrane-bound "cysteine-rich domain" (CRD)-NRG1 (Weickert et al., 2012), the predominant NRG1 isoform in the human brain (Liu et al., 2011). CRD-NRG1 serves as a key regulator of myelination in the peripheral nervous system (Nave and Salzer, 2006) but is not required for myelin assembly in the CNS (Brinkmann et al., 2008), suggesting that it has distinct functions in the brain.

Heterozygous disruption of CRD-NRG1 in mice results in deficits in glutamatergic and cholinergic neurotransmission from the hippocampus to the amygdala (Jiang et al., 2013; Zhong et al., 2008) and impaired short-term memory (Chen et al., 2008). Genetic inactivation of ErbB4, the predominant neuronal NRG1 receptor in the brain, results in increased long-term potentiation (LTP) (Pitcher et al., 2008) and blocked NRG1-mediated LTP

suppression in hippocampal slice culture (Chen et al., 2010). In addition, loss of ErbB4 in mice leads to impaired interneuron development, reduced GABAergic neurotransmission (Del Pino et al., 2013; Fazzari et al., 2010; Neddens and Buonanno, 2010), and enhanced limbic epileptogenesis (Li et al., 2012; Tan et al., 2012), demonstrating an important role of ErbB4 signaling in the regulation of inhibitory cortical circuitry. In ''gain-of-function'' approaches, the treatment of cultured neurons or brain slices with the soluble epidermal-growth-factor-like domain of NRG1 was shown to induce transcription of mRNAs encoding neurotransmitter receptors (Ozaki et al., 1997); to modulate glutamatergic, GABAergic, cholinergic, and dopaminergic neurotransmission (Gu et al., 2005; Kwon et al., 2005; Ting et al., 2011; Woo et al., 2007); to suppress hippocampal synaptic plasticity (Huang et al., 2000; Kwon et al., 2005; Pitcher et al., 2011); and to promote dendritic spine growth (Cahill et al., 2013). Recently, transgenic mice with forebrain-specific overexpression of ''soluble'' immunoglobulin (Ig)-domain-containing NRG1 (''Ig-NRG1'') have been reported to display synaptic dysfunction and behavioral deficits (Yin et al., 2013a). Collectively, these studies suggest that NRG1 functions as a pleiotropic factor in the establishment and fine-tuning of cortical circuitry. In addition, these data support the hypothesis that both reduced and increased NRG1 signaling may interfere with synaptic efficacy. However, the effect of elevated CRD-NRG1 signaling has not been studied in vivo, and due to embryonic lethality of the *Nrg1*-null mutation (Meyer and Birchmeier, 1995), the consequences of a permanent loss of NRG1 on synaptic functions have not been elucidated.

Here, we have modeled the loss of all NRG1 isoforms and elevated CRD-NRG1 expression in conditional mouse mutants and transgenic mice. Our data provide potential pathomechanisms for cortical disconnectivity in response to chronically altered CRD-NRG1 signaling.

RESULTS

Hypoactivity and Impaired Fear-Conditioned Learning in the Absence of NRG1

Postnatal recombination of a conditional (''floxed'') *Nrg1* allele (Li et al., 2002) in forebrain projection neurons using a *CamKII-Cre* driver line (Minichiello et al., 1999) resulted in a 30%–75% reduction of NRG1 protein levels in homozygous floxed *Nrg1* mutants harboring the *CamKII-Cre* transgene (referred to as *CK*Nrg1*$^{f/f}$), depending on the cortical region analyzed (Figures 1A, S1A, and S1B). Even at 18 months of age, we observed no signs of neurodegeneration and inflammation in the hippocampus (Figure 1B) or white matter (Figure S1C) and no change in the levels of PSD95, ErbB4, and several glutamate receptor subunits in *CK*Nrg1*$^{f/f}$ mutants (Figures 1C, 1D, and S1D).

Next, we performed a behavioral analysis of *CK*Nrg1*$^{f/f}$ mutants. We found no significant effects on the startle response and prepulse inhibition (PPI) in *CK*Nrg1*$^{f/f}$ mutants (Figures S1E and S1F; data not shown). However, *CK*Nrg1*$^{f/f}$ mutants displayed hypoactivity in the open-field test at 3 months of age (Figure 1E). Hypoactivity in *CK*Nrg1*$^{f/f}$ mutants was not associated with increased general anxiety in the open-field test (Figure S1G). Administration of the noncompetitive NMDA receptor antagonist MK-801 induces hyperactivity and serves as a pharmacological model of psychosis (Deutsch et al., 1997). A single dose of MK-801 (0.3 mg/kg) administered to control mice (*Nrg1*$^{f/+}$) at 3 months (Figure 1F) and 12 months of age (Figure 1H) increased motor activity for more than 1 hr. In contrast, *CK*Nrg1*$^{f/f}$ mutants at 3 to 4 months of age showed a strong tendency for reduced MK-801-induced hyperactivity (Figure 1F). At 12 months of age, *CK*Nrg1*$^{f/f}$ mutants were no longer hypoactive in the open-field test (Figure 1G). However, MK-801-induced hyperactivity was significantly reduced in *CK*Nrg1*$^{f/f}$ mutants and rapidly declined to baseline levels (Figure 1H). To examine the performance in a hippocampus-dependent learning task, we analyzed *CK*Nrg1*$^{f/f}$ mutants in a cued and contextual fear-conditioning paradigm. *CK*Nrg1*$^{f/f}$ mutants showed a tendency for reduced contextual fear conditioning at 3 to 4 months (Figure 1I) and exhibited a reduced freezing response both to the context and the auditory cue at 12 months of age (Figure 1J). Thus, loss of NRG1 signaling results in progressive deficits in hippocampus-dependent learning.

Loss of NRG1 Signaling Disrupts Synaptic Plasticity and Alters the Balance of Excitatory-Inhibitory Neurotransmission in the Hippocampus

To address whether reduced fear-conditioned learning in *CK*Nrg1*$^{f/f}$ mutants might result from impaired LTP, we tested field excitatory postsynaptic potentials (fEPSPs) at the Schaffer collateral (SC)-CA1 synapse of acute hippocampal slices from 18- to 20-month-old *CK*Nrg1*$^{f/f}$ mutant and *Nrg1*$^{f/+}$ control mice. No change in the input-output curve was observed (data not shown), but paired-pulse facilitation was reduced in *CK*Nrg1*$^{f/f}$ mutants (Figure 2A). Next, we induced synaptic potentiation in CA1 by high-frequency stimulation (HFS) of the SC. Short-term potentiation (STP) (1 min after HFS) was reduced, and the magnitude of LTP remained depressed 60 min after induction in *CK*Nrg1*$^{f/f}$ mutants (Figure 2B). To examine whether disrupted LTP was associated with changes in synaptic transmission already at younger age, we performed whole-cell patch-clamp recordings in CA1 pyramidal neurons. In 3-month-old *CK*Nrg1*$^{f/f}$ mutants, the amplitude of spontaneous excitatory postsynaptic currents (sEPSCs) was decreased (Figures 2C and 2D). Conversely, the amplitude of spontaneous inhibitory postsynaptic currents (sIPSCs) was increased (Figures 2F and 2G). Both sEPSC and sIPSC frequency were unchanged (Figures 2C, 2E, 2F, and 2H). In addition, the amplitude and frequency of miniature EPSCs (mEPSCs) were depressed in *CK*Nrg1*$^{f/f}$ mutants (Figures 2I–2K), whereas mIPSC amplitude was enhanced (Figures 2L and 2M) and mIPSC frequency was depressed (Figures 2L and 2N). In summary, postnatal NRG1 deficiency in projection neurons shifts the balance of excitatory-inhibitory neurotransmission toward enhanced inhibition and leads to reduced LTP in the hippocampus at later stages.

Embryonic NRG1 Signaling Is Not Essential for Interneuron Migration and the Formation of Inhibitory Cortical Circuits

To identify NRG1 functions during the establishment of neuronal circuits, we performed a subset of the above

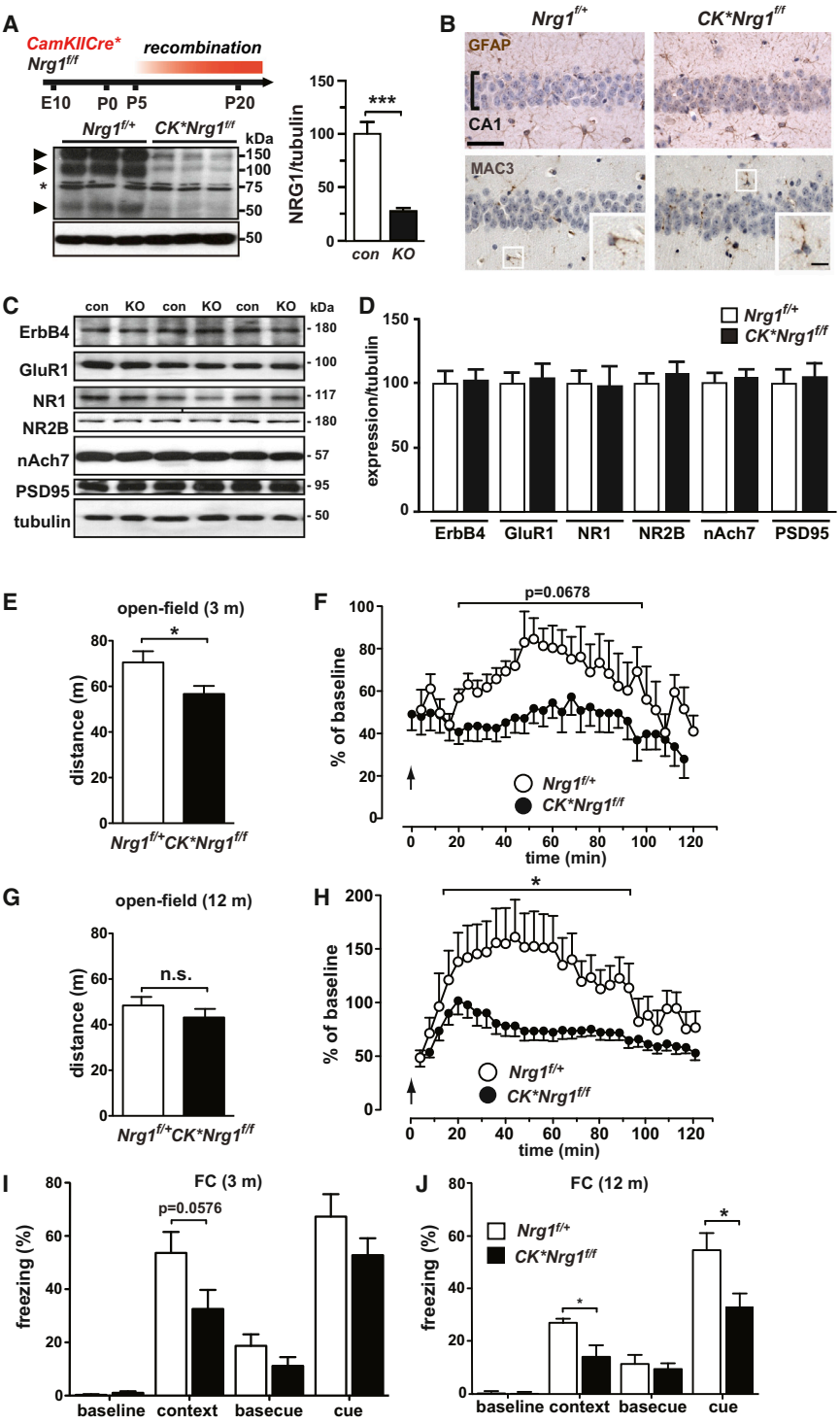

Figure 1. Behavioral Deficits in Mouse Mutants with a Postnatal Loss of NRG1 in Cortical Projection Neurons

(A) Time course of *Cre*-mediated NRG1 elimination in cortical projection neurons of *CamKCre*Nrg1$^{f/f}$* mutants. (Left) Western blot analysis of cortical protein lysates from mutants (*CK*Nrg1$^{f/f}$*) and controls (*Nrg1$^{f/+}$*; age 15 months). Arrowheads, full-length CRD-NRG1 (~140 kDa), Ig-NRG1 (~95 kDa), and C-terminal processing product (~60 kDa). Asterisk, unspecific protein band. (Right) Densitometric quantification of 140, 95, and 60 kDa NRG1 bands. Integrated density values were normalized to β-tubulin (n = 3/genotype; ***p < 0.0001).

(B) Immunostaining of *CK*Nrg1$^{f/f}$* mutants (12 months) shows absence of markers of inflammatory astrogliosis (GFAP) and microgliosis (MAC3) in the CA1 region (brackets). The scale bars represent 50 μm and 10 μm (inset).

(C) Western blot analysis of hippocampal protein lysates from *CK*Nrg1$^{f/f}$* mutants (knockout [KO]) and *Nrg1$^{f/+}$* controls (con) at 15 months after MK-801 treatment. ErbB4, ErbB4 receptor; GluR1, AMPA receptor subunit 1; NR1, NR2B, NMDA receptor subunit 1 and 2B; nAch7, nicotinic acetylcholine receptor α7 subunit; PSD95, postsynaptic density protein 95. β-tubulin was used as a loading control.

(D) Densitometric quantification of integrated density values normalized to β-tubulin (n = 3/genotype).

(E) Reduced motor activity of *CK*Nrg1$^{f/f}$* mutants (n = 15) in the open-field test compared with *Nrg1$^{f/+}$* controls (n = 10) at 3 months (*p < 0.05).

(F) Tendency for reduced responsiveness to MK-801 in *CK*Nrg1$^{f/f}$* mutants compared with *Nrg1$^{f/+}$* controls at 3 to 4 months. Motor activity in the open field was measured as the distance traveled during 4 min time intervals and expressed as percentage relative to baseline activity obtained individually before MK-801 treatment (single dose at 0.3 mg/kg). Arrow indicates MK-801 injection (*CK*Nrg1$^{f/f}$* n = 9; *Nrg1$^{f/+}$* n = 6; effect of genotype, p = 0.0678; two-way ANOVA for repeated measures).

(G) Unchanged motor activity of *CK*Nrg1$^{f/f}$* mutants (age 12 to 13 months) in the open-field test (n = 9–13). n.s., not significant.

(H) Reduced MK-801-induced hyperactivity in *CK*Nrg1$^{f/f}$* mutants compared with *Nrg1$^{f/+}$* controls at 12 to 13 months (n = 9–13; significant effect of genotype, $F_{(2, 696)} = 5.43$, *p < 0.05; significant effect of time, $F_{(29, 696)} = 7.08$, ***p < 0.0001; two-way ANOVA for repeated measures).

(I) Tendency for reduced contextual fear conditioning in *CK*Nrg1$^{f/f}$* mice in comparison to *Nrg1$^{f/+}$* controls at 3 to 4 months (n = 9–11; p = 0.0576). Fear-conditioned learning is displayed as the percentage of time mice show freezing behavior during a 2 min time period after re-exposure to context or cue (tone). Baseline: freezing during initial exposure to context prior to cue exposure. Base cue: freezing during exposure to new context prior to cue re-exposure. FC, fear conditioning.

(J) Reduced contextual and cued fear conditioning in *CK*Nrg1$^{f/f}$* mutant mice at 12 to 13 months (n = 9–12; *p < 0.05). Error bars represent SEM.

experiments in *Emx1-Cre*Nrg1$^{f/f}$* mutants (*Emx*Nrg1$^{f/f}$*), in which NRG1 is eliminated in projection neurons and glial cells beginning at embryonic day (E) 10 (Figure 3A; Gorski et al., 2002). *Emx*Nrg1$^{f/f}$* mutants were born at the expected Mendelian frequency and survived into adulthood. Despite a reduction of cortical NRG1 protein levels by ~80% in *Emx*Nrg1$^{f/f}$*

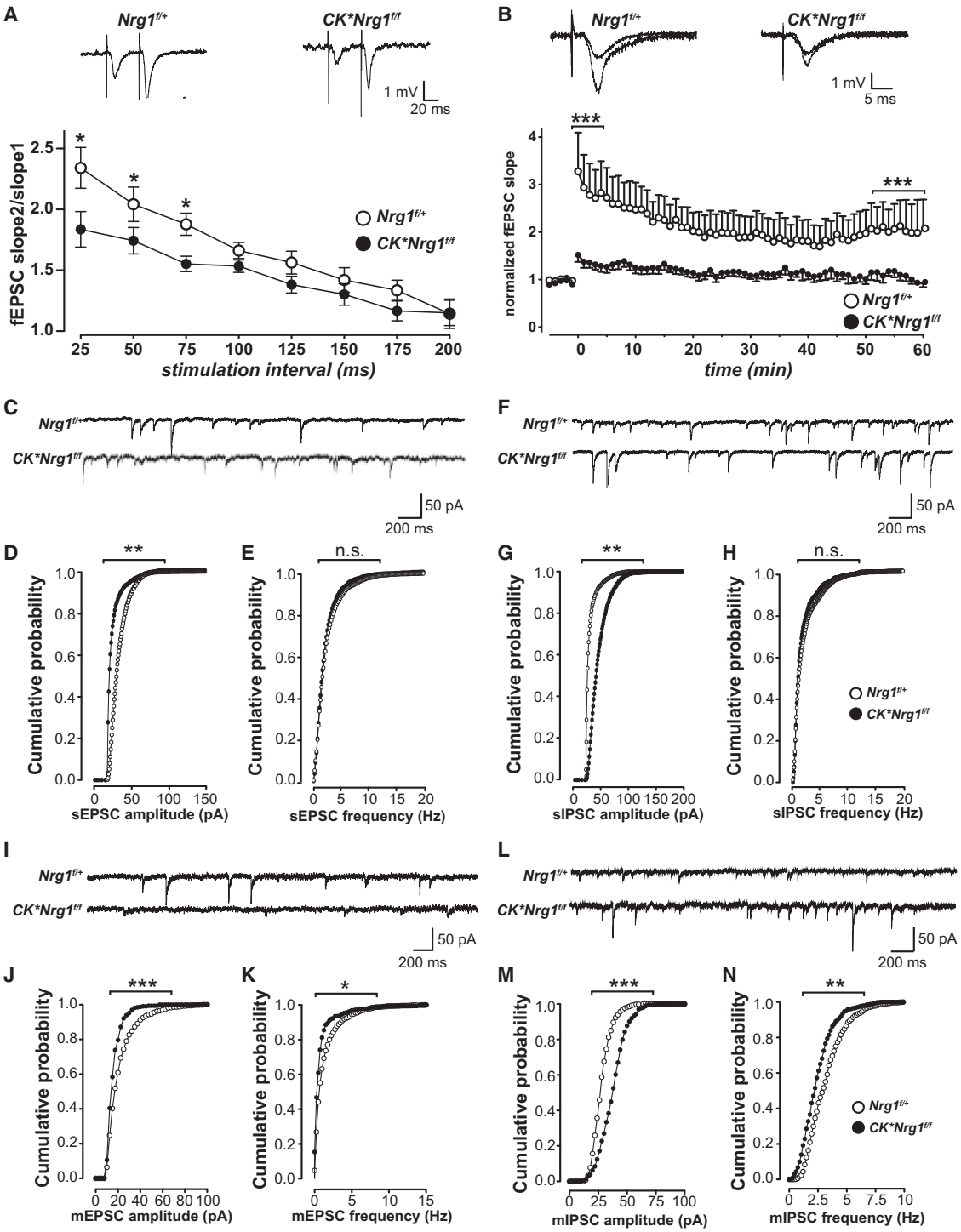

Figure 2. NRG1 Deficiency in Cortical Projection Neurons Disrupts Hippocampal Synaptic Plasticity and Increases Inhibitory Neurotransmission

(A) Top, sample fEPSPs traces from *CK*Nrg1*$^{f/f}$ mutant and *Nrg1*$^{f/+}$ control mice. Bottom, paired-pulse ratio (fEPSP slope second stimulus/fEPSP slope first stimulus) at interstimulus intervals of 25–75 ms was reduced in *CK*Nrg1*$^{f/f}$ mutants (n = 12) in comparison to *Nrg1*$^{f/+}$ controls (n = 11).

(B) Top, sample traces of responses before and after HFS. Bottom, LTP elicited by HFS (fEPSP slopes) for *CK*Nrg1*$^{f/f}$ mutants (n = 11) and *Nrg1*$^{f/+}$ controls (n = 12). HFS application at time point 0. Both the magnitude of STP (maximal responses within 1 min after HFS) and LTP (responses 50–60 min after HFS) were reduced in *CK*Nrg1*$^{f/f}$ mice.

(C) Representative sEPSC recordings from CA1 pyramidal neurons of a *CK*Nrg1*$^{f/f}$ mutant and *Nrg1*$^{f/+}$ control.

(legend continued on next page)

mutants (Figure 3B), gray and white matter structures appeared to be normally developed (Figures S2A and S2C). In contrast to ErbB4 mutants (Neddens and Buonanno, 2010), the number of GAD67-positive cells in the hippocampus (Figures 3C and 3E) and their cortical-layer-specific distribution (Figures 3D, 3F, and S2D) were not altered in *Emx*Nrg1*$^{f/f}$ mutants at postnatal day (P) 14.

Whole-cell patch-clamp recordings of CA1 pyramidal neurons revealed changes in neurotransmission in 3-month-old *Emx*Nrg1*$^{f/f}$ mutants similar to findings in *CK*Nrg1*$^{f/f}$ mutants. The amplitude of sEPSCs was depressed (Figures 3G–3I), whereas both sIPSC amplitude and frequency (***$p < 0.001$) were increased in *Emx*Nrg1*$^{f/f}$ mutants (Figures 3J–3L). Similarly, mEPSC amplitude was reduced (Figures 3M–3O) and mIPSC amplitude enhanced in *Emx*Nrg1*$^{f/f}$ mutants (Figures 3P–3R).

These findings argue against an essential role for glial and projection neuron-derived NRG1 during interneuron migration and the formation of inhibitory cortical circuits but support NRG1 functions in the fine tuning of excitatory and inhibitory neurotransmission in projection neurons.

Elevated CRD-NRG1 Expression Increases Inhibitory Neurotransmission and Disrupts Synaptic Plasticity in the Hippocampus

CRD-NRG1 is the most prominent NRG1 variant in the mature cortex (Liu et al., 2011). To test the hypothesis that CRD-NRG1 serves as a signal for ErbB-receptor-mediated synaptic tuning, we examined transgenic mice (*Nrg1-tg*) that express CRD-NRG1 from the neuronal Thy1.2 promoter (Michailov et al., 2004). Transgene expression was initiated around E16 (Figure S2B) and prominent in neocortex and hippocampus of the adult brain (Figures 4A and 4B). CRD-NRG1 accumulated on the surface of projection neurons but was absent from interneurons, astrocytes, and oligodendrocytes (Figure 4C). Western blot analysis revealed increased steady-state levels of phosphorylated ErbB4 receptor in the hippocampus of *Nrg1-tg* mice at 4 months of age (Figure 4D). Thus, *Nrg1-tg* mice model chronically elevated CRD-NRG1 expression (derived from cortical projection neurons) and ErbB4 receptor hyperphosphorylation beginning at late embryonic stages.

In the absence of markers of neurodegeneration and inflammation (Figure S2C), we performed in vivo MRI and found that lateral ventricular volume was reduced in *Emx*Nrg1*$^{f/f}$ mutants and increased in *Nrg1-tg* mice, whereas total brain volume was not changed at 12 months of age (Figures 4E–4G and S3F). Ventricular volume was already increased in 6-month-old *Nrg1-tg* mice (Figures S3C–S3E), but not at P14 (Figures S3A and S3B), suggesting a young adult onset. Thus, ventricular enlargement, a condition frequently observed in schizophrenia patients, is associated with elevated CRD-NRG1 expression, but not with NRG1 deficiency in our mouse models.

Next, we studied synaptic transmission in CA1 pyramidal neurons of *Nrg1-tg* mice and wild-type littermate controls (wild-type [*WT*]). Both sEPSC amplitude and frequency were unaltered in *Nrg1-tg* mice (Figures 5A–5C). In contrast, sIPSC frequency was almost doubled in *Nrg1-tg* mice (Figures 5D–5F). Similarly, mEPSC amplitude and frequency were unaltered (Figures S4A and S4B), whereas mIPSC frequency was enhanced in *Nrg1-tg* mice (Figures 5G and 5H). When we examined LTP at the SC-CA1 synapse, we observed no changes in the input-output curve or paired-pulse facilitation (Figure S4C); however, both STP and LTP were reduced in *Nrg1-tg* mice (Figure 5I). These findings suggest that elevated CRD-NRG1 signaling shifts the excitatory-inhibitory synaptic balance in CA1 pyramidal neurons toward enhanced inhibition, most likely due to increased synaptic input from GABAergic interneurons and/or enhanced presynaptic GABA release.

To address whether impaired LTP was related to changes in the molecular composition of cortical synapses, we prepared cortical synaptosomes from *Nrg1-tg* mice, *Emx*Nrg1*$^{f/f}$ mutants, and controls. Western blot analyses identified differences in the synaptic levels of CRD-NRG1 in *Nrg1-tg* mice in comparison to *Emx*Nrg1*$^{f/f}$ mutant mice, but protein levels for ErbB4, PSD95, as well as GluN1 and GluN2B subunits of NMDA receptors were not changed (Figures 5J and S5A), consistent with the unaltered transcription of ErbB4 and various neurotransmitter receptors (Figures S5B–S5E). To obtain global protein expression profiles from *Nrg1-tg* mice, we analyzed their proteome using a label-free shotgun-liquid chromatography-mass spectrometry (LC-MS^{E}) approach. This resulted in the identification of 40 differentially expressed proteins in the hippocampus of 4-month-old *Nrg1-tg* mice (see Table S1), including several that play a role in functional and structural plasticity at glutamatergic synapses (CaM kinase II α and β subunits, protein phosphatase 2B, and septin 6; Figure 5K). Next, we identified interaction networks and canonical pathways using the Ingenuity Pathways KnowledgeBase (IPKB) (http://www.ingenuity.com). A significant network showed interactions of the uploaded proteins with a cluster of glutamate receptors (Figure 5L; Table S2). The most significant canonical pathway was LTP (not shown; $p < 0.001$), consistent with our electrophysiological findings in *Nrg1-tg* mice.

(D and E) Cumulative probability plots of sEPSC amplitude (D) and frequency (E) in CA1 pyramidal neurons from *CK*Nrg1*$^{f/f}$ mutants (n = 6) and *Nrg1*$^{f/+}$ controls (n = 8).
(F) Representative sIPSC recordings from CA1 pyramidal neurons of a *CK*Nrg1*$^{f/f}$ mutant and *Nrg1*$^{f/+}$ control.
(G and H) Cumulative probability plots of sIPSC amplitude (G) and frequency (H) in CA1 pyramidal neurons from *CK*Nrg1*$^{f/f}$ mutant (n = 8) and *Nrg1*$^{f/+}$ control (n = 5) mice.
(I) Representative mEPSC recordings from CA1 pyramidal neurons of a *CK*Nrg1*$^{f/f}$ mutant and *Nrg1*$^{f/+}$ control.
(J and K) Cumulative probability plots of mEPSC amplitude (J) and frequency (K) in CA1 pyramidal neurons from *CK*Nrg1*$^{f/f}$ mutants (n = 6) and *Nrg1*$^{f/+}$ controls (n = 8).
(L) Representative mIPSC recordings from CA1 pyramidal neurons of a *CK*Nrg1*$^{f/f}$ mutant and *Nrg1*$^{f/+}$ control.
(M and N) Cumulative probability plots of sIPSC amplitude (M) and frequency (N) in CA1 pyramidal neurons from *CK*Nrg1*$^{f/f}$ mutant (n = 9) and *Nrg1*$^{f/+}$ control (n = 10) mice. *$p < 0.05$; **$p < 0.01$; ***$p < 0.001$; Mann-Whitney U test.

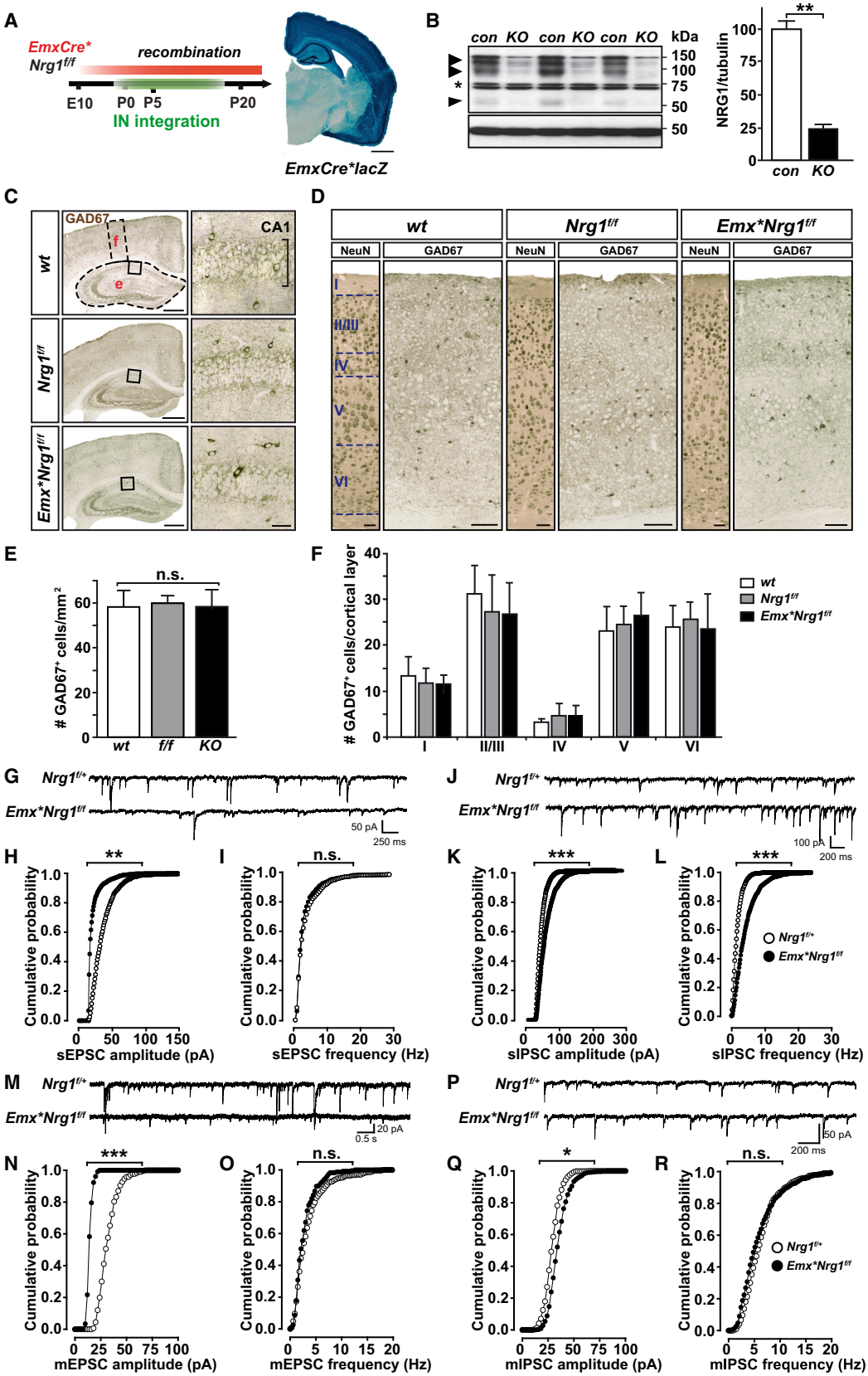

(legend on next page)

Abnormal Spine Growth and Reduced Numbers of Parvalbumin-Expressing Interneurons in the Neocortex of *Nrg1-tg* Mice

We next addressed whether increased CRD-NRG1 expression also affects neocortical network functions. To visualize dendrites and spines, we crossbred *Nrg1-tg* mice with a *Thy1.2-YFP* transgenic mouse line, which expresses yellow fluorescent protein (YFP) in a subset of projection neurons in cortical layer V (Hirrlinger et al., 2005). In vivo imaging of dendrites in *Thy1.2-YFP*Nrg1-tg* double transgenic mice (*YFP*Nrg1*) and *Thy1.2-YFP* controls (con) at 3 to 4 months of age by two-photon laser-scanning microscopy (2P-LSM) revealed no difference in the number of primary dendrites (*con:* 7.24 ± 0.17; *YFP*Nrg1:* 7.18 ± 0.09; Figures 6A, 6B, and S6C) and branch points of apical dendrites up to the marginal zone (MZ) (*con:* 4.03 ± 0.32; *YFP*Nrg1:* 4.23 ± 0.22; Figures 6A and 6C). Next, we applied stimulated emission depletion (STED) nanoscopy through a cranial window above the somatosensory cortex to resolve structural details of apical dendrites and spines of layer V projection neurons in the MZ of live mice (Berning et al., 2012). Total spine frequency was not changed in *YFP*Nrg1* mice (*con:* 0.35 ± 0.02 μm^{-1}, *YFP*Nrg1:* 0.36 ± 0.02 μm^{-1}; Figure 6D). Using in vivo STED nanoscopy, we observed several previously defined morphological spine classes ("mushroom," "cup," "stubby," "filopodium," and "bifurcated"; Hering and Sheng, 2001; Trommald et al., 1996) and determined their frequency (Figures S6A and S6B). In *YFP*Nrg1* mice, the frequency of bifurcated spines was increased more than 3-fold (*con*: set as 1 ± 0.31; *YFP*Nrg1*: 3.74 ± 0.82; $p < 0.01$), and we observed a concomitant, albeit not significant, reduction in the frequency of other spine types, except for filopodium-like spines (Figure 6E). Furthermore, the necks of mushroom and cup spines were longer in *YFP*Nrg1* mice compared with controls (*mushroom*: *con*: 0.98 ± 0.04 μm, *YFP*Nrg1*: 1.2 ± 0.05 μm, $p < 0.05$; *cup*: *con*: 1.05 ± 0.06 μm, *YFP*Nrg1*: 1.27 ± 0.02 μm, $p < 0.05$; Figure 6F).

To assess functional consequences of the selective increase of bifurcated spines, we performed recordings in cortical layer V neurons using acute cortical slices prepared from the same neocortical area that was used for in vivo STED nanoscopy. Both mEPSC frequency and amplitude were increased in *YFP-Nrg1* mice (Figures 6G–6I). In addition, analysis of mEPSC kinetics revealed that the mean slope of onset was increased and the distribution shifted toward events with faster onset in *YFP-Nrg1* mice (*con*: 12.77 ± 0.23 pA/ms; *YFP-Nrg1*: 18.24 ± 0.26 pA/ms; Figure 6J). Given that perisomatic events display faster onset in comparison to dendritic events (Miles et al., 1996), these data suggest that changes in spine structure may reduce effective glutamatergic synaptic transmission by changing the NMDA/AMPA ratio or postsynaptic receptor kinetics at distal sites.

CRD-NRG1 serves as a permissive signal for the migration of cortical interneurons in vitro (Flames et al., 2004), suggesting that interneuron migration could be affected in *Nrg1-tg* mice. Immunostaining for GAD67 and parvalbumin (PV) at P14 revealed minor changes in the cortical distribution of $GAD67^+$ cells in *Nrg1-tg* mice (Figure 7A), but not in the total number of neocortical (Figures 7A and 7B) and hippocampal interneurons (Figures S6D and S6E). To visualize PV^+ interneurons in vivo, we crossbred *Nrg1-tg* mice with *PV-GFP* transgenic mice that express GFP under control of regulatory sequences from the *PV* gene (Meyer et al., 2002). 2P-LSM in vivo imaging of *PV-GFP*Nrg1-tg* double transgenic mice at 3 months of age revealed a lower number of GFP^+ cells in cortical layers II/III and V and a reduction in the total number of GFP^+ cells by ~20% compared with *PV-GFP* controls (Figures 7C and 7D). We observed a similar reduction of GFP^+ cells in a second mouse line, which expresses epitope-tagged CRD-NRG1 (Velanac et al., 2012). PV^+

Figure 3. Embryonic NRG1 Signaling Is Not Essential for Interneuronal Migration

(A) Embryonic NRG1 elimination using the *Emx1-Cre* driver line overlaps with network integration of cortical interneurons (IN). X-gal histochemistry on brain section from an *Emx-Cre*Rosa26lacZ* double-transgenic mouse (P46) shows Cre-mediated recombination of *lacZ* reporter in forebrain projection neurons and glial cells. The scale bar represents 1 mm.

(B) (Left) Western blot analysis of cortical protein extracts from *Emx*Nrg1$^{f/f}$* mutants (KO) and *Nrg1$^{f/+}$* con at 4 months. Arrowheads, full-length and processed NRG1 protein. Asterisk, unspecific protein band. (Right) Densitometric quantification of NRG1 isoforms (140 and 95 kDa). Integrated density values were normalized to β-tubulin (n = 3/genotype; $^{**}p < 0.01$).

(C) Normal numbers and cortical positions of $GAD67^+$ interneurons in *Emx*Nrg1$^{f/f}$* mutants during cortical maturation. Immunostaining for GAD67 on coronal brain sections from *Emx*Nrg1$^{f/f}$* mutants and controls (*Nrg1$^{f/f}$* and *WT*) at P14. Higher magnifications (right) show the hippocampal CA1 region (boxed in overviews). The scale bars represent 500 μm and 50 μm (CA1 region).

(D) Immunostaining for NeuN and GAD67 (higher magnification of boxed area f in C) reveals normal layering (I–VI, cortical layers) and interneuron positions in the somatosensory cortex of *Emx*Nrg1$^{f/f}$* mutants in comparison to controls (*Nrg1$^{f/f}$* and *WT*). Bregma, −1.7; scale bars, 50 μm (NeuN); 100 μm (GAD67).

(E) Quantification of $GAD67^+$ interneurons in the hippocampus (marked area e in C) of *Emx*Nrg1$^{f/f}$* mutants and controls (*Nrg1$^{f/f}$* and *WT*). n = 6/genotype.

(F) Quantification of $GAD67^+$ interneurons in the neocortex (boxed area f in C) of *Emx*NRG1$^{f/f}$* mutants and controls (*Nrg1$^{f/f}$* and *WT*). n = 6/genotype. Error bars represent SEM.

(G) Representative sEPSC recordings of CA1 pyramidal neurons from *Emx*NRG1$^{f/f}$* mutants and *Nrg1$^{f/+}$* controls.

(H and I) Cumulative probability plots of sEPSC amplitude (H) and frequency (I) in CA1 pyramidal neurons from *Emx*Nrg1$^{f/f}$* mutants (n = 9) and *Nrg1$^{f/+}$* controls (n = 8).

(J) Representative sIPSC recordings of pyramidal neurons from *Emx*NRG1$^{f/f}$* mutants and *Nrg1$^{f/+}$* controls.

(K and L) Cumulative probability plots of sIPSC amplitude (K) and frequency (L) in pyramidal neurons from *Emx*Nrg1$^{f/f}$* mutants (n = 6) and *Nrg1$^{f/+}$* controls (n = 7).

(M) Representative mEPSC recordings of pyramidal neurons from *Emx*NRG1$^{f/f}$* mutants and *Nrg1$^{f/+}$* controls.

(N and O) Cumulative probability plots of mEPSC amplitude (N) and frequency (O) in pyramidal neurons from *Emx*Nrg1$^{f/f}$* mutants (n = 8) and *Nrg1$^{f/+}$* controls (n = 5).

(P) Representative mIPSC recordings of pyramidal neurons from *Emx*NRG1$^{f/f}$* mutants and *Nrg1$^{f/+}$* controls.

(Q and R) Cumulative probability plots of mIPSC amplitude (Q) and frequency (R) in pyramidal neurons from *Emx*Nrg1$^{f/f}$* mutants (n = 10) and *Nrg1$^{f/+}$* controls (n = 10).

$^{*}p < 0.05$; $^{**}p < 0.01$; $^{***}p < 0.001$; Mann–Whitney U test.

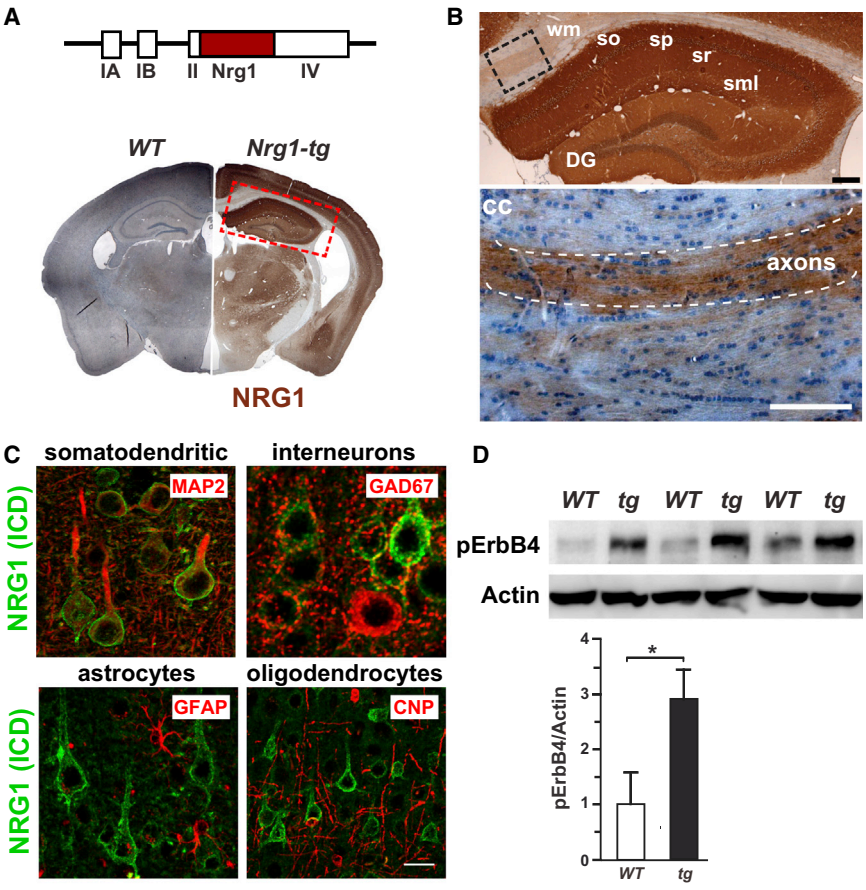

Figure 4. Elevated CRD-NRG1 Expression Causes Ventricular Enlargement

(A) Neuronal CRD-NRG1 overexpression in transgenic mice. Structure of the Thy1.2 transgene cassette (brown box, CRD-NRG1 cDNA; white boxes, exons I-IV of the Thy1.2 gene). Immunostaining for NRG1 on coronal brain sections from wild-type (*WT*) and CRD-NRG1 transgenic mice (*Nrg1-tg*) at 12 months. Note enlarged lateral ventricle in *Nrg1-tg* brain.

(B) Top, CRD-NRG1 expression in hippocampal pyramidal neurons and granule cells of *Nrg1-tg* mice (magnification of boxed area in A). Bottom, CRD-NRG1 is present in callosal axons (magnification of boxed area at the top). cc, corpus callosum; DG, dentate gyrus; sml, stratum moleculare; so, stratum oriens; sp, stratum pyramidale; sr, stratum radiatum; wm, white matter. The scale bars represent 125 μm (top) and 60 μm (bottom).

(C) Projection neuron-specific CRD-NRG1 overexpression. Confocal images of coronal brain sections after fluorescent immunostaining for NRG1 (green) and markers (red) for projection neurons (MAP2), interneurons (GAD67), astrocytes (GFAP), and oligodendrocytes (CNP) in the somatosensory cortex of *Nrg1-tg* mice. The scale bar represents 20 μm.

(D) Chronic ErbB4 hyperphosphorylation in the hippocampus of *Nrg1-tg* mice. Western blot analysis of hippocampal protein lysates from *Nrg1-tg* mice (*tg*) and WT (4 months). Densitometric quantification of phosphorylated ErbB4 bands. Integrated density values were normalized to β-actin (n = 3/genotype; *$p < 0.05$; two-tailed t test).

(E) Enlarged lateral ventricles in *Nrg1-tg* mice (arrowheads) in comparison to *Emx*Nrg1$^{f/f}$* mutants and *WT* mice (12 to 13 months). T1-weighted MRI.

(F) MRI-based volumetric analysis reveals no changes in total brain volume (cm^3) of *Emx*Nrg1$^{f/f}$* mutants and *Nrg1-tg* in comparison to *WT* mice (n = 5 per genotype; Mann-Whitney U test).

(G) Ventricular volume (in percent of total brain volume) is reduced in *Emx*Nrg1$^{f/f}$* mutants and increased in *Nrg1-tg* in comparison to *WT* mice (*WT, Emx*Nrg1$^{f/f}$*, n = 5; *Nrg1-tg,* n = 4; **$p < 0.01$, WT versus *Emx*Nrg1$^{f/f}$*; $p < 0.05$, *WT* versus *Nrg1-tg* and *Emx*f/f* versus *Nrg1-tg*; Mann-Whitney U test).

interneurons provide perisomatic inhibition to projection neurons. Electrophysiological recordings in acute cortical slices (as above) revealed a moderate increase in mIPSC frequency in layer V projection neurons (Figures 7E–7G). Analysis of mIPSC kinetics showed a shift toward events with slower onset, such that the mean slope of event onset was reduced in *Nrg1-tg* mice (con: 27.9 ± 0.34 pA/ms; *Nrg1-tg*: 22.8 ± 0.18 pA/ms; Figure 7H), consistent with a reduction of PV^+ interneuron-mediated perisomatic events in layer V.

Finally, we tested whether increased CRD-NRG1 expression causes behavioral dysfunctions. The neuromuscular junction in *Nrg1-tg* mice is severely compromised (W.J. Thompson, personal communication), which renders these mice less suitable for behavioral analysis. Therefore, we examined a mouse line (*HA-Nrg1-tg*), in which hemagglutinin (HA) epitope-tagged CRD-NRG1 is expressed under control of the same Thy1.2 cassette as in *Nrg1-tg* mice

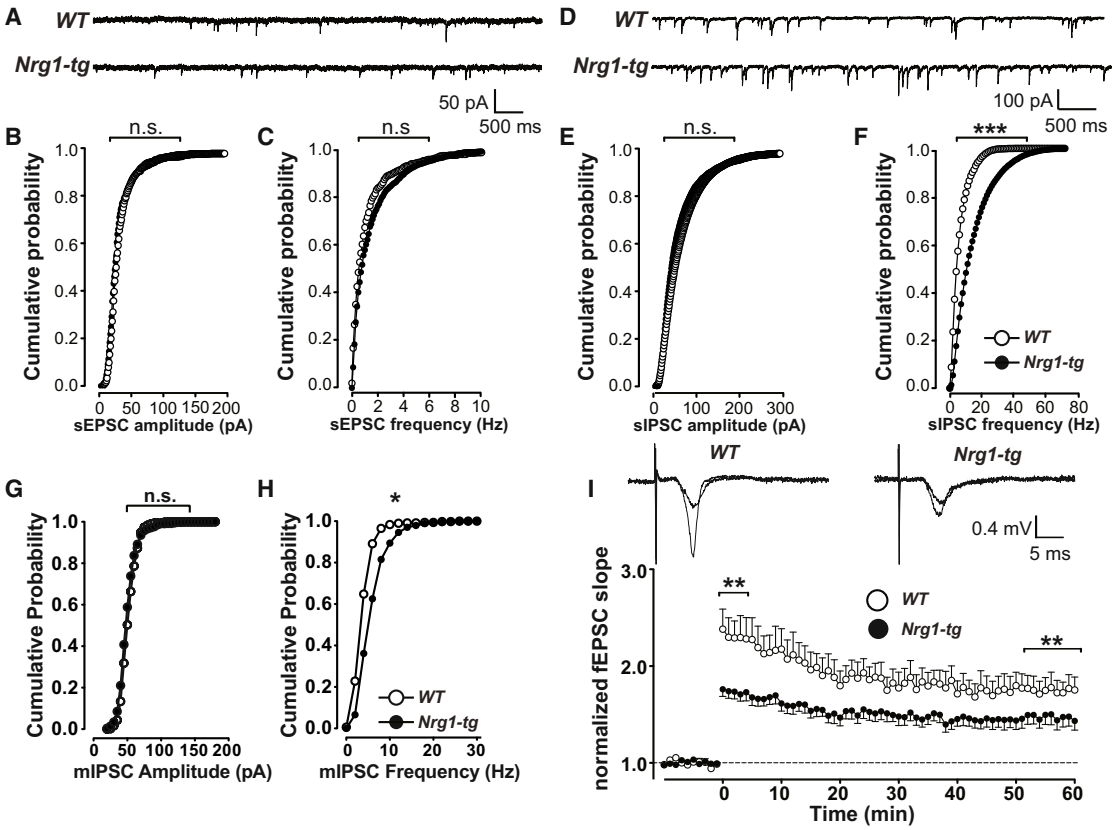

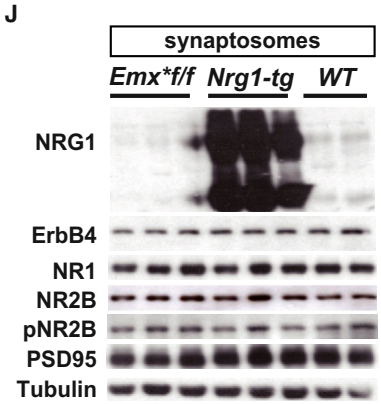

K

Acc	Protein	Ratio	Pep	Wilco
Cell signalling				
P11798	CaM kinase II alpha chain	0.67	51	0.0304
P28652	CaM kinase II beta chain	0.77	43	0.0304
P48454	Ser/Thr-protein phosphatase 2B	1.23	6	0.0141
P97813	Phospholipase D2	1.43	2	0.0304
Cytoskeleton/ECM				
Q9QYR6	Microtubule-associated protein 1A	1.10	37	0.0304
Q9R1T4	Septin 6	0.82	2	0.0464
Q99KJ8	Dynactin subunit 2	0.77	3	0.0102
Q62059	Versican core protein	0.80	2	0.0043
Ion transport				
Q924N4	Solute carrier family 12 member 6	1.15	19	0.0120
Q5DTL9	Na-driven Cl-bicarbonate exchanger	1.27	8	0.0262

L

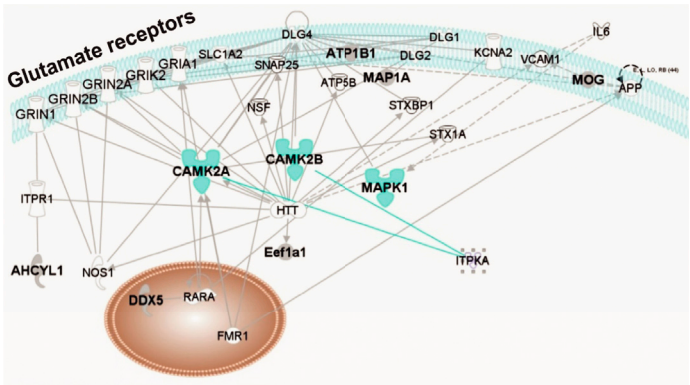

(legend on next page)

(Figure S7A; Velanac et al., 2012). Similar to *Nrg1-tg* mice, we observed HA-CRD-NRG1 expression on the surface of cortical projection neurons, ventricular enlargement, and a reduced number of GFP+ interneurons in *HA-Nrg1-tg* mice (Figures S7B–S7D). At 2 to 3 months of age, the distance traveled in the open-field test was not altered in *HA-Nrg1-tg* mice (m; males: *WT*: 44.17 ± 1.93, *HA-Nrg1-tg*: 42.49 ± 2.21; females: *WT*: 42.92 ± 1.41, *HA-Nrg1-tg*: 42.31 ± 2.32; Figure S7E). However, *HA-Nrg1-tg* mice spent less time in the center of the open-field arena (males: *WT*: 24.16% ± 3.77%, *HA-Nrg1-tg*: 10.61% ± 2.13%; females: *WT*: 21.11% ± 2.11%, *HA-Nrg1-tg*: 6.87% ± 2.41%; Figure 7I) and male mice displayed more frequent defecation (males: *WT*: 1.778 ± 0.586; *HA-Nrg1-tg*: 4.13 ± 0.72; Figure S7F), in line with increased anxiety. In addition, *HA-Nrg1-tg* mice performed fewer rearings (males: *WT*: 56.28 ± 3.86, *HA-Nrg1-tg*: 39 ± 4.64; females: *WT*: 48.5 ± 2.92, *HA-Nrg1-tg*: 31.1 ± 4.53; Figure 7J), suggesting diminished exploratory behavior. Assessment of sensorimotor gating (Figures 7K and 7L) showed a profound PPI deficit in *HA-Nrg1-tg* mice. Moreover, they displayed an increased startle response (males: *WT*: 184.9 ± 39.56, *HA-Nrg1-tg*: 344.9 ± 42.07; females: *WT*: 71.43 ± 12.51, *HA-Nrg1-tg*: 280.2 ± 19.24; Figure S7G). In summary, our findings in loss- and gain-of-function mouse mutants support a bell-shaped model of NRG1-mediated synaptic functions (Figure 8), according to which an optimal level of NRG1 signaling is required for balanced synaptic transmission and plasticity in the cortex.

DISCUSSION

In this study, we carried out a systematic characterization of conditional *Nrg1* mutants and *Nrg1-tg* mice with increased CRD-NRG1 expression. The main findings of this study are as follows: (1) Both NRG1 deficiency and increased CRD-NRG1 expression led to disrupted hippocampal plasticity and imbalanced excitatory and inhibitory neurotransmission. (2) Elevated CRD-NRG1 expression resulted in ventricular enlargement and abnormal spine growth. (3) Morphological changes in *Nrg1-tg* mice were accompanied by increased anxiety levels and disrupted sensorimotor gating.

Our analysis of *CK*Nrg1*$^{f/f}$ mutants has shown that NRG1 is required for hippocampal LTP. This finding contrasts with a study in heterozygous *Nrg1* mutants, in which hippocampal LTP was increased (Shamir et al., 2012). These discrepancies most likely reflect differences in the spatiotemporal profile of *Nrg1* deletion in conventional heterozygous mutants in comparison to conditional *Nrg1*-null mutants and point to the modulatory role of distinct levels of NRG1 during synaptic transmission. In addition, loss of NRG1 in *CK*Nrg1*$^{f/f}$ and *Emx*Nrg1*$^{f/f}$ mutant mice consistently resulted in increased IPSC amplitudes in hippocampal pyramidal neurons. We conclude that expression or responsiveness of postsynaptic GABA receptors on pyramidal neurons is enhanced in the absence of NRG1 signaling. Our findings in *Nrg1* conditional mutants contrast with those in *ErbB4*-null mutants, in which inhibitory circuits are compromised (Del Pino et al., 2013; Fazzari et al., 2010; Neddens and Buonanno, 2010; Wen et al., 2010) and LTP is enhanced (Chen et al., 2010; Pitcher et al., 2008; Shamir et al., 2012). Thus, we suggest that NRG1 is an important, but not the sole, mediator of ErbB4 signaling in the brain and that ErbB4 integrates signals from multiple ligands, such as neuregulin 2 (Carraway et al., 1997), during the regulation of inhibitory circuits.

Similar to NRG1 deficiency, elevated CRD-NRG1 expression in projection neurons disrupted hippocampal LTP. In addition, we observed increased IPSC frequency and abnormal spine growth in pyramidal cells of CRD-NRG1 transgenic mice. These effects appeared to be specific for CRD-NRG1 as overexpression of Ig-domain-containing NRG1 (Ig-NRG1 or NRG1 type I) in transgenic mice using the same Thy1.2 promoter led to impaired gamma oscillation, whereas LTP formation was not affected (Deakin et al., 2012). A distinct transgenic mouse line with forebrain-specific overexpression of Ig-NRG1 shows reduced mEPSC frequency and mIPSC amplitudes but unaltered mIPSC frequency (Yin et al., 2013a). These data suggest that CRD-NRG1, mainly acting via juxtacrine signaling, and Ig-NRG1, serving as a soluble ligand in paracrine signaling, provide distinct functions in the modulation of excitatory and inhibitory neurotransmission. Together, our data demonstrate an imbalance in the excitatory/inhibitory (E/I) ratio toward pronounced inhibition in conditional *Nrg1* mutants and CRD-NRG1 transgenic mice. We speculate that alterations in the E/I ratio in response to altered NRG1 signaling could lead to deficits in cortical synchronization, as implicated in schizophrenia (Uhlhaas and Singer, 2010).

Figure 5. Elevated CRD-NRG1 Expression Increases Inhibitory Neurotransmission and Disrupts Hippocampal Plasticity

(A) Representative sEPSC recordings from CA1 pyramidal neurons in *WT* and *Nrg1-tg* mice (3 to 4 months).

(B and C) Cumulative probability plots of sEPSC amplitude (B) and frequency (C) in pyramidal neurons from *Nrg1-tg* mice (n = 15) compared with *WT* (n = 10).

(D) Representative sIPSC recordings from pyramidal neurons in *WT* and *Nrg1-tg* mice.

(E and F) Cumulative probability plots of sIPSC amplitude (E) and frequency (F) in pyramidal neurons from *WT* (n = 9) and *NRG1-tg* mice (n = 16).

(G and H) Cumulative probability plots of mIPSC amplitude (G) and frequency (H) in pyramidal neurons from *WT* (n = 8) and *NRG1-tg* mice (n = 9). *p < 0.05; **p < 0.01; ***p < 0.001; Mann-Whitney U test.

(I) Sample traces of responses (top) before and after HFS and LTP elicited by HFS. fEPSP slopes from *Nrg1-tg* mice (n = 22) were in comparison to *WT* mice (n = 15). Both STP and LTP were significantly reduced in *Nrg1-tg* mice (**p < 0.01; Student's t test).

(J) Western blot analysis of proteins (Triton X-100 soluble and insoluble fraction of synaptosomal lysates) prepared from cerebral cortices of *Emx*Nrg1*$^{f/f}$ mutant, *Nrg1-tg*, and *WT* mice (age 15–18 months). Levels of ErbB4, NR1, NR2B, phosphorylated NR2B (pNR2B), and PSD95 were unaltered in all genotypes. Note: β-tubulin cosediments in all fractions as a contaminant.

(K) LC-MS^{E} identification of differentially expressed proteins in the hippocampus of *Nrg1-tg* (n = 10) in comparison to *WT* (n = 10) mice. Acc, UniProt accession code; ECM, extracellular matrix; Pep, number of peptides identified for each protein; Ratio, *Nrg1-tg/WT* for each protein; Wilco, Wilcoxon test.

(L) Accession codes for altered proteins (see Table S1) were uploaded into the Ingenuity Pathways KnowledgeBase (IPKB). This led to identification of a significant network (score 15), which showed interactions of the uploaded proteins with other proteins in the IPKB (see Table S2). CAMK2A, CAMK2B, and mitogen-activated protein kinase 1 (MAPK1) kinases are highlighted in blue. A cluster of five glutamate receptors predicted to interact with the uploaded proteins is also indicated.

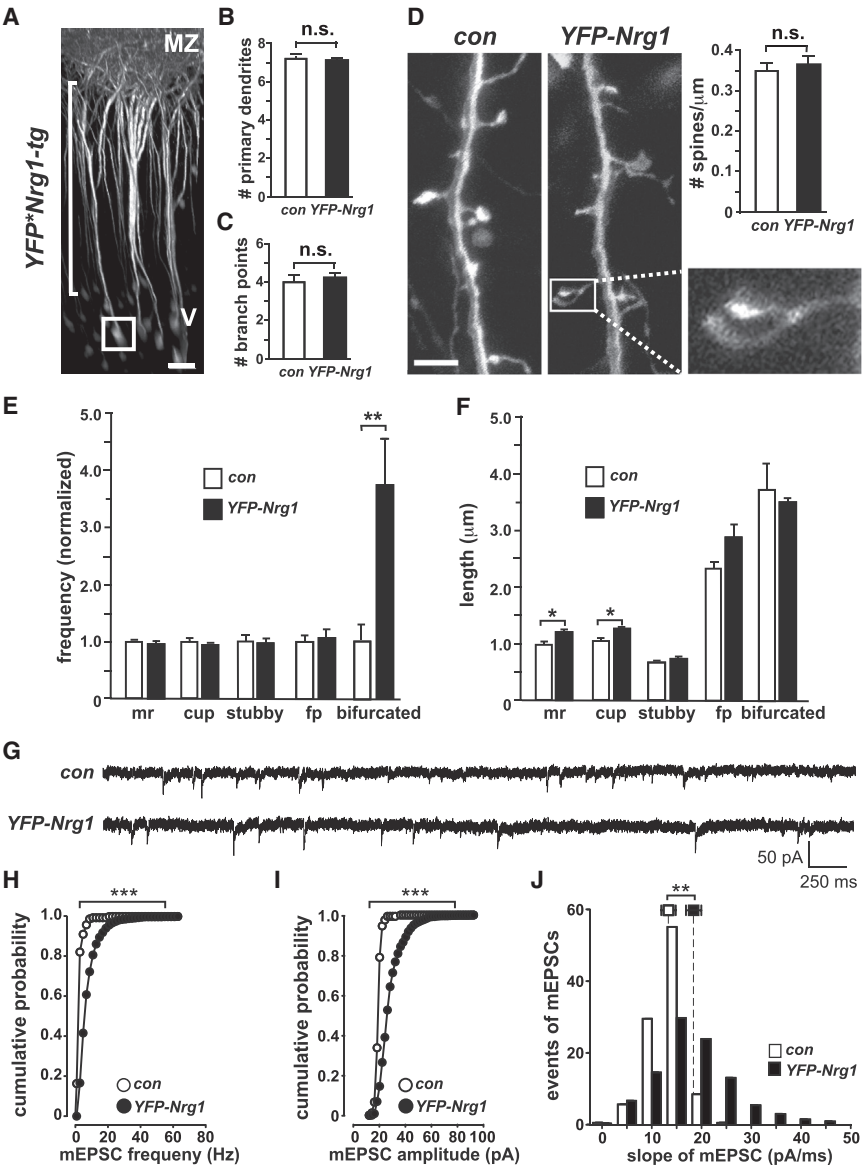

Figure 6. Abnormal Spine Growth in *Nrg1-tg* Mice

(A) 2P-LSM imaging of cortical layer V projection neurons. Fluorescent image stacks were recorded in *Thy1.2-YFP*Nrg1-tg* (*YFP-Nrg1*) and *Thy1.2-eYFP* (*con*) mice at 3 to 4 months. 3D volume of the somatosensory cortex (bregma −2) from the marginal zone (MZ) to layer V, rendered from fluorescent image stacks. Box and bracket indicate areas used for quantification in (B) and (C). The scale bar represents 40 µm.

(B) The number of primary dendrites (quantified in boxed area in A) was not altered in *YFP*Nrg1* compared with control mice (n = 10 neurons/mouse; n = 7 mice/genotype).

(C) The number of apical dendrite branch points (from cell soma in layer V to the MZ, indicated by bracket in A) was not altered in *YFP*NRG1* mice compared with control mice (n = 10 neurons/mouse; n = 7 mice/genotype).

(D) In vivo STED nanoscopy of dendrites in the MZ derived from cortical layer V projection neurons of a con and a *YFP*Nrg1* mouse. A bifurcated-type spine (boxed) is shown at higher magnification. The scale bar represents 2 µm.

(E) Relative frequency of spine classes (controls set as 1) in the MZ of *YFP-Nrg1* mice and controls (30 dendrites per mouse; con, n = 4 mice; *YFP-Nrg1*, n = 3, $^{**}p < 0.01$; one way ANOVA, post hoc Tukey's test). fp, filopodium; mr, mushroom.

(F) Length (µm) of spine neck (for mushroom, cup, and bifurcated spines) or entire spine (stubby and filopodium). Necks of mushroom- and cup-like spines were longer in *YFP-Nrg1* mice (30 dendrites/mouse; *con*, n = 4 mice; *YFP-Nrg1*, n = 3; $^{*}p < 0.05$; $^{**}p < 0.01$; one-way ANOVA; post hoc Tukey's test). Error bars represent SEM.

(G) Representative recordings of glutamatergic mEPSCs from YFP^+ projection neurons in cortical layer V of control and *YFP-Nrg1* mice.

(H and I) Cumulative probabilities of mEPSC frequencies (H) and amplitudes (I) in YFP^+ neurons from control (n = 12) and *YFP-Nrg1* (n = 13) mice. $^{**}p < 0.01$; $^{***}p < 0.001$; Mann-Whitney U test.

(J) Onset kinetics expressed as normalized histograms of rise slopes (peak amplitude in pA over time of onset in ms) of glutamatergic mEPSCs. Mean values and the significance of onset kinetics are indicated by squares positioned relative to the x axis. $^{**}p < 0.01$; Mann-Whitney U test.

Based on the phenotypic profile of CRD-NRG1 overexpressing mice, we suggest that human NRG1 risk haplotypes exert a gain-of-function effect. This hypothesis is supported by the finding that the schizophrenia risk haplotype HapICE is associated with increased CRD-NRG1 expression in the prefrontal cortex (Weickert et al., 2012). In addition, elevated CRD-NRG1 expression induced chronic ErbB4 hyperphosphorylation in the cortex of CRD-NRG1 transgenic mice, consistent with findings in postmortem brain from schizophrenia patients (Hahn et al., 2006). We propose that elevated CRD-NRG1 signaling impairs synaptic plasticity via two mechanisms. First, it alters the cortical E/I ratio. Specifically, we hypothesize that increased juxtacrine signaling by CRD-NRG1 during development hyperstimulates ErbB4 receptors in PV^+ interneurons, which increases feedforward inhibition by promoting the formation of GABAergic presynaptic terminals on pyramidal neurons, as indicated by elevated IPSC frequency. Increased feedforward inhibition could compromise LTP formation. Second, it induces abnormal spine growth. Elevated expression levels of CRD-NRG1 result in its accumulation in the somatodendritic compartment of pyramidal neurons. This could initiate abnormal backsignaling, such as aberrant interactions of the C-terminal domain of NRG1 with LIM kinase 1 (Wang et al., 1998; Yin et al., 2013a), a major regulator of spine growth (Mizuno, 2013). Whereas we favor this model, ErbB4 expressed in projection neurons and interneurons was shown to regulate spine growth (Cooper and Koleske, 2014;

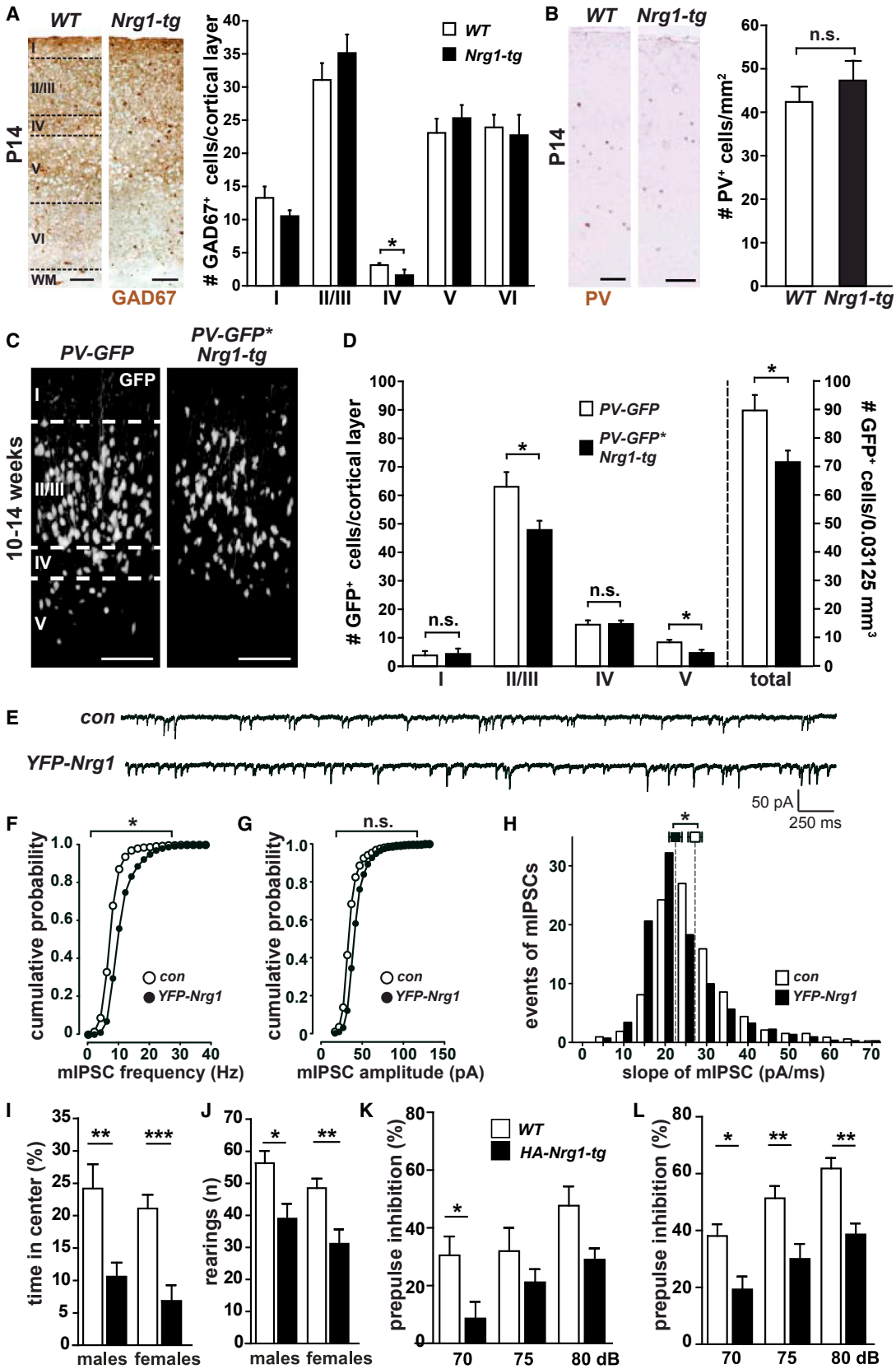

(legend on next page)

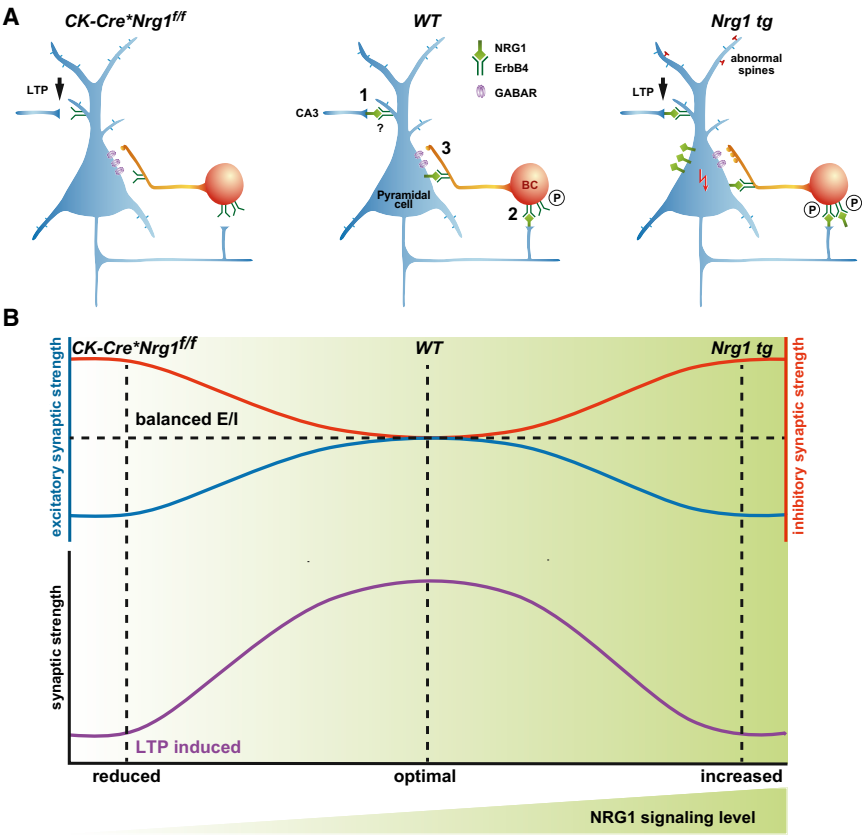

Figure 8. Bell-Shaped Model of NRG1-Mediated Signaling in the Cortex

(A) Middle, sites of possible NRG1/ErbB4 interactions in a simple microcircuit of the hippocampal CA1 region in wild-type. (1) Excitatory CA3/CA1 (Schaffer collateral) synapse. (2) Excitatory pyramidal cell synapse on inhibitory (PV^+) basket cell (BC). (3) Inhibitory BC synapse on pyramidal cell. Question mark indicates uncertain ErbB4 expression in pyramidal cells. Left, absence of pyramidal cell-derived NRG1 signaling (*CK*Nrg1*$^{f/f}$ mutant mice) leads to LTP impairment at the CA1/CA3 synapse and increased IPSC amplitudes, consistent with elevated expression/function of GABA receptors. Right, CRD-NRG1 overexpression in pyramidal cells (*Nrg1-tg* mice) promotes ErbB4 hyperphosphorylation and inhibitory synapse formation/function in BC (as indicated by increased IPSC frequency) and leads to impaired LTP at the CA1/CA3 synapse and abnormal spine growth. LTP and spine defects may result, at least in part, from somatodendritic CRD-NRG1 accumulation and aberrant "back-signaling" (red flash), partly independent from ErbB4.

(B) Both chronically reduced and increased levels of NRG1 signaling cause enhanced inhibitory synaptic strength and reduced excitatory synaptic strength, leading to a dysbalanced E/I ratio and impaired hippocampal LTP.

Del Pino et al., 2013; Yin et al., 2013b). Thus, abnormal spine morphology could directly result from chronic hyperstimulation of ErbB4 receptors. In summary, our data support the hypothesis that abnormal spine growth, observed in schizophrenia patients (Penzes et al., 2011), could be induced by hyperstimulated CRD-NRG1 signaling.

Ventricular enlargement is the most-replicated endophenotype in schizophrenia, and variants of the *NRG1* gene are associated with increased lateral ventricle volume in schizophrenia patients (Mata et al., 2009). We observed reduced ventricular size in *Emx*Nrg1*$^{f/f}$ mutants but enlarged lateral ventricles in *Nrg1-tg* mice. Ventricular size is not affected in Ig-NRG1 transgenic mice (P. Harrison, personal communication). These findings suggest a specific role of CRD-NRG1 in the regulation of ventricular volume. Thus, chronically increased CRD-NRG1 expression could represent a risk factor for ventricular enlargement observed in schizophrenia patients.

In summary, our in vivo data demonstrate that both chronically reduced and increased NRG1 signaling interferes with balanced neurotransmission and synaptic plasticity. Our

Figure 7. Disturbed Inhibitory Circuitry, Anxiety-like Behavior, and Reduced PPI in *Nrg1-tg* Mice

(A) (Left) Immunostaining for GAD67 on coronal brain sections from *WT* and *Nrg1-tg mice* at P14 (somatosensory cortex; bregma −1.7). The scale bars represent 100 μm. (Right) Quantification of $GAD67^+$ interneurons (n = 6/genotype; *p < 0.05, Mann-Whitney U test). I–VI, cortical layers; WM, white matter.

(B) (Left) Immunostaining for PV as in (A). The scale bars represent 100 μm. (Right) Quantification of PV^+ interneurons across all cortical layers (n = 6/genotype; Mann-Whitney U test).

(C) 2P-LSM of *PV-GFP*Nrg1-tg* and *PV-GFP* control mice. Depicted are 3D projections-rendered live-imaging stacks of a cortical column (250 × 250 × 500 μm^3; 2 μm stack interval) from the MZ to layer V.

(D) Quantification of GFP^+ interneurons in layers I–V from 2P-LSM live-imaging stacks. Note that parts of layers V and VI could not be imaged. *PV-GFP*Nrg1-tg*, n = 6; *PV-GFP*, n = 5; *p < 0.05; Student's t test.

(E) Representative recordings of GABAergic mIPSCs from YFP^+ projection neurons in layer V of *Thy1.2-YFP*Nrg1-tg* (*YFP-Nrg1*) and *Thy1.2-YFP* (*con*) mice.

(F and G) Cumulative probabilities of mIPSC frequencies (F) and amplitudes (G) in YFP^+ neurons from *YFP-Nrg1* (n = 17) and control (n = 15) mice.

(H) Onset kinetics expressed as normalized histograms of rise slopes (peak amplitude in pA over time to onset in ms) of GABAergic mIPSCs. Mean values and the significance of onset kinetics are indicated by squares positioned relative to the x axis. *p < 0.05; Mann-Whitney U test.

(I) *HA-Nrg1-tg* mice (age 2 to 3 months) spent less time in the center of the open-field arena when compared with *WT*.

(J) *HA-Nrg1-tg* mice performed less rearings than *WT* in the open-field test.

(K and L) Reduced PPI in male (K) and female (L) *HA-Nrg1-tg* mice. Males: effect of genotype $F_{(1,32)} = 4.31$; *p < 0.05 for prepulse 70 dB; females: effect of genotype $F_{(1,24)} = 16.09$; ***p < 0.001; two-way ANOVA; Bonferroni posttest. (I–L): *WT*: males, n = 18; females, n = 18; *HA-Nrg1-tg* mice: males, n = 16; females, n = 10. Error bars represent SEM.

findings extend an "inverted U" model of NRG1 signaling (Role and Talmage, 2007), and we propose a bell-shaped model, according to which an "optimal" level of NRG1 is required for the establishment, refinement, and "homeostasis" of synaptic neurotransmission. Although chronically reduced NRG1 signaling in the brain impairs synaptic functions, our data suggest that it is chronically increased CRD-NRG1 signaling that phenocopies several endophenotypes described for schizophrenia patients. Thus, CRD-NRG1 transgenic mice could provide a robust preclinical model for further studies of schizophrenia and to facilitate the discovery and development of treatment strategies.

EXPERIMENTAL PROCEDURES

Transgenic and Mutant Mice

The generation and genotyping of conditional *null* mutants of *Nrg1* (Li et al., 2002) and transgenic lines CRD-NRG1 (Michailov et al., 2004), HA-CRD-NRG1 (Velanac et al., 2012), PV-GFP (Meyer et al., 2002), Emx1-Cre (Gorski et al., 2002), and CamKIIα-Cre (Minichiello et al., 1999) has been described. Primer sequences are available upon request. All animal experiments were carried out in compliance with approved animal policies of the Max Planck Institute of Experimental Medicine.

RNA Analysis

Total RNA was extracted using Qiazol Reagent (QIAGEN). cDNA was synthesized from total RNA using random nonamer primers and Superscript III RNase H reverse transcriptase (Invitrogen). Quantitative real-time PCR was carried out using the ABI Prism 7700 Sequence Detection System as described (Brinkmann et al., 2008) and analyzed with 7500 Fast System SDS software version 1.3 (Applied Biosystems) and GraphPad Prism 5.0. PCR primer sequences are available upon request.

Protein Analysis

Brain tissue was homogenized in sucrose or radioimmunoprecipitation assay buffer with protease inhibitors (Complete tablets; Roche). For western blotting, 5–50 μg of protein lysate was size separated on 8% SDS-polyacrylamide gels and blotted onto polyvinylidene fluoride membranes (Hybond-P; Invitrogen) according to manufacturer's instructions. Membranes were incubated with primary antibodies as described in Supplemental Experimental Procedures. The densitometric analysis of scanned enhanced chemiluminescence films was carried out using ImageJ and GraphPad Prism 5.0. Data are displayed as SEM, and statistical significance was tested using a Mann-Whitney U test.

Synaptosomes and Synaptic Plasma Membrane Preparation

Synaptosomes were isolated by a sucrose density gradient technique (Dodd et al., 1981) modified to isolate synaptosomes from small quantities of starting material (detailed in Supplemental Experimental Procedures). Synaptosomes were fractionated into Triton X-100 soluble (synaptic membranes) and insoluble (mainly postsynaptic density proteins) fractions by ultracentrifugation (Mizoguchi et al., 1989). The Triton X-100 insoluble fraction was solubilized using 2% SDS buffer. Analysis was performed using SDS-PAGE and western blotting as described above and in Supplemental Experimental Procedures.

Proteomics

Proteins were extracted from hippocampal tissue, followed by separation on SDS-polyacrylamide gels and enzymatic digestion with trypsin. Resulting peptides were analyzed on a Waters quadrupole time-of-flight Premier mass spectrometer as described (Martins-de-Souza et al., 2007). Wilcoxon signed-rank tests were used to determine statistical significance ($p < 0.05$).

Histology and Immunostaining

Free-floating vibratome (40–50 μm) or paraffin sections (5 μm) were incubated overnight with primary antibodies as described in Supplemental Experimental Procedures. Sections were incubated with secondary antibodies Cy2 (1:10,000; Jackson ImmunoResearch), Cy3 (1:10,000; Jackson ImmunoResearch), Alexa 488 and Alexa Fluor 555 (1:2,000; Invitrogen) for 1 hr at room temperature. For the analysis of neurodegenerative changes, paraplast-embedded sections (5–7 μm) were stained with hematoxylin and eosin staining (Merck) and Cresyl Violet. Digital images were obtained using 510-meta LSM and Axiophot (Zeiss) and DMRXA (Leica) microscopes. All images were processed with ImageJ.

Electrophysiology

Transverse slices (300 μm) were cut from mouse brain (10–12 weeks old) and transferred to a recording chamber filled with artificial cerebrospinal fluid. Field recording data were digitized by DigiData 1322A and analyzed using Clampfit 10.0 (Molecular Devices). During whole-cell patch recordings, sIPSCs were recorded at a holding potential of -70 mV in the presence of 10 μM 6-cyano-7-nitroquinoxaline-2,3-dione and 40 μM 2-amino-5-phosphonopentanoic acid; sEPSCs were recorded in the presence of 5 μM strychnine and 5 μM bicuculline. For mIPSC and mEPSC recording, 0.5 μM tetrodotoxin was added to the bath solution. Data acquisition and analysis was carried out using pClamp 10.0 (Molecular Devices), MiniAnalysis (SynaptoSoft), and Prism 4 (GraphPad). Statistical significance was evaluated using a two-tailed unpaired Student's t test with Welch's correction or a Mann-Whitney U test. Significance level was set to $p < 0.05$, and values are displayed as SEM. For details, see the Supplemental Experimental Procedures.

MRI and Volumetry

Mice were anesthetized with 5% isofluorane, intubated, and kept under anesthesia with 1%–1.5% isofluorane in oxygen and ambient air (1:1.5). MRI was performed at a field strength of 2.35 T (Bruker Biospin MRI) using a T1-weighted 3D FLASH sequence as described (Natt et al., 2002), reaching an isotropic resolution of 117 μm. Total brain volume (excluding olfactory bulb, cerebellum, and brainstem) and, separately, the size of the lateral and third ventricles, cerebellum, olfactory bulb, and brainstem were determined by manually drawing respective regions of interest on up to 50 contiguous horizontal MRI sections.

In Vivo 2P-LSM and In Vivo STED Nanoscopy

Two-photon microscopy (Agarwal et al., 2012) and STED imaging (Berning et al., 2012) were performed as described. See the Supplemental Experimental Procedures for details.

Behavioral Testing

For behavioral experiments, age-matched *CK-Cre*Nrg1*$^{f/f}$, *CK-Cre*Nrg1*$^{f/+}$, *Nrg1*$^{f/+}$, *HA-Nrg1-tg*, and WT mice at 12–15 weeks of age were used. Three to five mice per cage were housed in a room with a 12 hr light-dark cycle (lights on at 9:00 a.m.) with ad libitum access to food and water. Behavioral tests were conducted in a blinded fashion during the light phase (10:00 a.m.–5:00 p.m.) as described in Brzózka et al. (2010). Data are displayed as SEM, and statistical significance was analyzed using a Mann-Whitney U test and a two-way ANOVA with Bonferroni posttest (for multiple group comparisons). See the Supplemental Experimental Procedures for details. All experiments were performed with permission from the local Animal Care and Use Committee (Bezirksregierung Braunschweig) in accordance with the German Animal Protection Law.

SUPPLEMENTAL INFORMATION

Supplemental Information includes Supplemental Experimental Procedures, seven figures, and four tables and can be found with this article online at http://dx.doi.org/10.1016/j.celrep.2014.07.026.

AUTHOR CONTRIBUTIONS

A.A. generated *CamKII-Cre*Nrg1* and *Emx1-Cre*Ngr1* mice and carried out biochemical, histological and gene expression analysis on NRG1 conditional mutants and transgenic mice. M.Z., I.T.-D., Z.T., and W.Z. performed electrophysiological analysis. T.U. contributed to histological, biochemical, and behavioral analysis of *Emx1-Cre*Nrg1* mutants and transgenic mice. K.R.,

T.U., M.M.B., M.J.R., and H.E. carried out behavioral analysis. M.N.G. generated *HA-Nrg1* transgenic mice. A.A., S. Boretius, and J.F. performed MRI-based volumetric analysis. P.D. performed in vivo 2P-LSM. S. Berning, H.S., K.I.W., and S.W.H. were responsible for STED imaging. D.M.d.S., P.C.G., and S. Bahn carried out proteomic analysis. K.-A.N. and H.E. contributed conceptual ideas and supervised experiments. A.A., W.Z., and M.H.S. designed the study, analyzed data, and wrote the manuscript. All authors read and approved the final manuscript.

ACKNOWLEDGMENTS

We thank A. Fahrenholz and M. Floerl for excellent technical assistance. We also thank C. Casper and D. Flemming for help with animal husbandry. We thank C. Birchmeier for providing conditional NRG1 mutant mice, R. Klein for CamKII-Cre mice, K. Jones for EmxI-Cre mice, F. Kirchhoff for Thy1.2-YFP mice, and H. Monyer for PV-GFP mice. We thank N. Brose, S. Papiol, S. Wichert, and members of the Department of Neurogenetics for helpful discussions. A.A. is supported by a Postdoctoral Fellowship from the National Multiple Sclerosis Society. W.Z. is supported by the IZKF of the University of Münster Medical School (Zha3-005-14). M.J.R. and M.M.B. were supported by the Deutsche Forschungsgemeinschaft (Klinische Forschergruppe [KFO] 241: RO 4076/1-1). S.W.H., W.Z., M.H.S., and K.-A.N. acknowledge grant support from the Deutsche Forschungsgemeinschaft (DFG Research Center Molecular Physiology of the Brain [CMPB] and SFB TRR58 to W.Z.). M.H.S. is supported by a Heisenberg fellowship from the Deutsche Forschungsgemeinschaft. K.-A.N. holds an ERC Advanced Grant.

Received: November 25, 2013
Revised: April 4, 2014
Accepted: July 16, 2014
Published: August 14, 2014

REFERENCES

Agarwal, A., Dibaj, P., Kassmann, C.M., Goebbels, S., Nave, K.A., and Schwab, M.H. (2012). In vivo imaging and noninvasive ablation of pyramidal neurons in adult NEX-CreERT2 mice. Cereb. Cortex *22*, 1473–1486.

Ayalew, M., Le-Niculescu, H., Levey, D.F., Jain, N., Changala, B., Patel, S.D., Winiger, E., Breier, A., Shekhar, A., Amdur, R., et al. (2012). Convergent functional genomics of schizophrenia: from comprehensive understanding to genetic risk prediction. Mol. Psychiatry *17*, 887–905.

Berning, S., Willig, K.I., Steffens, H., Dibaj, P., and Hell, S.W. (2012). Nanoscopy in a living mouse brain. Science *335*, 551.

Bertram, I., Bernstein, H.G., Lendeckel, U., Bukowska, A., Dobrowolny, H., Keilhoff, G., Kanakis, D., Mawrin, C., Bielau, H., Falkai, P., and Bogerts, B. (2007). Immunohistochemical evidence for impaired neuregulin-1 signaling in the prefrontal cortex in schizophrenia and in unipolar depression. Ann. N Y Acad. Sci. *1096*, 147–156.

Brinkmann, B.G., Agarwal, A., Sereda, M.W., Garratt, A.N., Müller, T., Wende, H., Stassart, R.M., Nawaz, S., Humml, C., Velanac, V., et al. (2008). Neuregulin-1/ErbB signaling serves distinct functions in myelination of the peripheral and central nervous system. Neuron *59*, 581–595.

Brzózka, M.M., Radyushkin, K., Wichert, S.P., Ehrenreich, H., and Rossner, M.J. (2010). Cognitive and sensorimotor gating impairments in transgenic mice overexpressing the schizophrenia susceptibility gene Tcf4 in the brain. Biol. Psychiatry *68*, 33–40.

Cahill, M.E., Remmers, C., Jones, K.A., Xie, Z., Sweet, R.A., and Penzes, P. (2013). Neuregulin1 signaling promotes dendritic spine growth through kalirin. J. Neurochem. *126*, 625–635.

Carraway, K.L., 3rd, Weber, J.L., Unger, M.J., Ledesma, J., Yu, N., Gassmann, M., and Lai, C. (1997). Neuregulin-2, a new ligand of ErbB3/ErbB4-receptor tyrosine kinases. Nature *387*, 512–516.

Chen, Y.J., Johnson, M.A., Lieberman, M.D., Goodchild, R.E., Schobel, S., Lewandowski, N., Rosoklija, G., Liu, R.C., Gingrich, J.A., Small, S., et al. (2008). Type III neuregulin-1 is required for normal sensorimotor gating, memory-related behaviors, and corticostriatal circuit components. J. Neurosci. *28*, 6872–6883.

Chen, Y.J., Zhang, M., Yin, D.M., Wen, L., Ting, A., Wang, P., Lu, Y.S., Zhu, X.H., Li, S.J., Wu, C.Y., et al. (2010). ErbB4 in parvalbumin-positive interneurons is critical for neuregulin 1 regulation of long-term potentiation. Proc. Natl. Acad. Sci. USA *107*, 21818–21823.

Cooper, M.A., and Koleske, A.J. (2014). Ablation of ErbB4 from excitatory neurons leads to reduced dendritic spine density in mouse prefrontal cortex. J. Comp. Neurol. *522*, 3351–3362.

Deakin, I.H., Nissen, W., Law, A.J., Lane, T., Kanso, R., Schwab, M.H., Nave, K.A., Lamsa, K.P., Paulsen, O., Bannerman, D.M., and Harrison, P.J. (2012). Transgenic overexpression of the type I isoform of neuregulin 1 affects working memory and hippocampal oscillations but not long-term potentiation. Cereb. Cortex *22*, 1520–1529.

Del Pino, I., García-Frigola, C., Dehorter, N., Brotons-Mas, J.R., Alvarez-Salvado, E., Martínez de Lagrán, M., Ciceri, G., Gabaldón, M.V., Moratal, D., Dierssen, M., et al. (2013). Erbb4 deletion from fast-spiking interneurons causes schizophrenia-like phenotypes. Neuron *79*, 1152–1168.

Deutsch, S.I., Rosse, R.B., and Mastropaolo, J. (1997). Behavioral approaches to the functional assessment of NMDA-mediated neural transmission in intact mice. Clin. Neuropharmacol. *20*, 375–384.

Dodd, P.R., Hardy, J.A., Oakley, A.E., Edwardson, J.A., Perry, E.K., and Delaunoy, J.P. (1981). A rapid method for preparing synaptosomes: comparison, with alternative procedures. Brain Res. *226*, 107–118.

Falls, D.L. (2003). Neuregulins: functions, forms, and signaling strategies. Exp. Cell Res. *284*, 14–30.

Fazzari, P., Paternain, A.V., Valiente, M., Pla, R., Luján, R., Lloyd, K., Lerma, J., Marín, O., and Rico, B. (2010). Control of cortical GABA circuitry development by Nrg1 and ErbB4 signalling. Nature *464*, 1376–1380.

Flames, N., Long, J.E., Garratt, A.N., Fischer, T.M., Gassmann, M., Birchmeier, C., Lai, C., Rubenstein, J.L., and Marín, O. (2004). Short- and long-range attraction of cortical GABAergic interneurons by neuregulin-1. Neuron *44*, 251–261.

Gorski, J.A., Talley, T., Qiu, M., Puelles, L., Rubenstein, J.L., and Jones, K.R. (2002). Cortical excitatory neurons and glia, but not GABAergic neurons, are produced in the Emx1-expressing lineage. J. Neurosci. *22*, 6309–6314.

Gu, Z., Jiang, Q., Fu, A.K., Ip, N.Y., and Yan, Z. (2005). Regulation of NMDA receptors by neuregulin signaling in prefrontal cortex. J. Neurosci. *25*, 4974–4984.

Hahn, C.G., Wang, H.Y., Cho, D.S., Talbot, K., Gur, R.E., Berrettini, W.H., Bakshi, K., Kamins, J., Borgmann-Winter, K.E., Siegel, S.J., et al. (2006). Altered neuregulin 1-erbB4 signaling contributes to NMDA receptor hypofunction in schizophrenia. Nat. Med. *12*, 824–828.

Hering, H., and Sheng, M. (2001). Dendritic spines: structure, dynamics and regulation. Nat. Rev. Neurosci. *2*, 880–888.

Hirrlinger, P.G., Scheller, A., Braun, C., Quintela-Schneider, M., Fuss, B., Hirrlinger, J., and Kirchhoff, F. (2005). Expression of reef coral fluorescent proteins in the central nervous system of transgenic mice. Mol. Cell. Neurosci. *30*, 291–303.

Huang, Y.Z., Won, S., Ali, D.W., Wang, Q., Tanowitz, M., Du, Q.S., Pelkey, K.A., Yang, D.J., Xiong, W.C., Salter, M.W., and Mei, L. (2000). Regulation of neuregulin signaling by PSD-95 interacting with ErbB4 at CNS synapses. Neuron *26*, 443–455.

Jiang, L., Emmetsberger, J., Talmage, D.A., and Role, L.W. (2013). Type III neuregulin 1 is required for multiple forms of excitatory synaptic plasticity of mouse cortico-amygdala circuits. J. Neurosci. *33*, 9655–9666.

Kwon, O.B., Longart, M., Vullhorst, D., Hoffman, D.A., and Buonanno, A. (2005). Neuregulin-1 reverses long-term potentiation at CA1 hippocampal synapses. J. Neurosci. *25*, 9378–9383.

Law, A.J., Lipska, B.K., Weickert, C.S., Hyde, T.M., Straub, R.E., Hashimoto, R., Harrison, P.J., Kleinman, J.E., and Weinberger, D.R. (2006). Neuregulin 1 transcripts are differentially expressed in schizophrenia and regulated by 5′ SNPs associated with the disease. Proc. Natl. Acad. Sci. USA *103*, 6747–6752.

Li, L., Cleary, S., Mandarano, M.A., Long, W., Birchmeier, C., and Jones, F.E. (2002). The breast proto-oncogene, HRGalpha regulates epithelial proliferation and lobuloalveolar development in the mouse mammary gland. Oncogene *21*, 4900–4907.

Li, D., Collier, D.A., and He, L. (2006). Meta-analysis shows strong positive association of the neuregulin 1 (NRG1) gene with schizophrenia. Hum. Mol. Genet. *15*, 1995–2002.

Li, K.X., Lu, Y.M., Xu, Z.H., Zhang, J., Zhu, J.M., Zhang, J.M., Cao, S.X., Chen, X.J., Chen, Z., Luo, J.H., et al. (2012). Neuregulin 1 regulates excitability of fast-spiking neurons through Kv1.1 and acts in epilepsy. Nat. Neurosci. *15*, 267–273.

Liu, X., Bates, R., Yin, D.M., Shen, C., Wang, F., Su, N., Kirov, S.A., Luo, Y., Wang, J.Z., Xiong, W.C., and Mei, L. (2011). Specific regulation of NRG1 isoform expression by neuronal activity. J. Neurosci. *31*, 8491–8501.

Martins-de-Souza, D., Menezes de Oliveira, B., dos Santos Farias, A., Horiuchi, R.S., Crepaldi Domingues, C., de Paula, E., Marangoni, S., Gattaz, W.F., Dias-Neto, E., and Camillo Novello, J. (2007). The use of ASB-14 in combination with CHAPS is the best for solubilization of human brain proteins for two-dimensional gel electrophoresis. Brief. Funct. Genomic Proteomic *6*, 70–75.

Mata, I., Perez-Iglesias, R., Roiz-Santiañez, R., Tordesillas-Gutierrez, D., Gonzalez-Mandly, A., Vazquez-Barquero, J.L., and Crespo-Facorro, B. (2009). A neuregulin 1 variant is associated with increased lateral ventricle volume in patients with first-episode schizophrenia. Biol. Psychiatry *65*, 535–540.

Meyer, D., and Birchmeier, C. (1995). Multiple essential functions of neuregulin in development. Nature *378*, 386–390.

Meyer, A.H., Katona, I., Blatow, M., Rozov, A., and Monyer, H. (2002). In vivo labeling of parvalbumin-positive interneurons and analysis of electrical coupling in identified neurons. J. Neurosci. *22*, 7055–7064.

Michailov, G.V., Sereda, M.W., Brinkmann, B.G., Fischer, T.M., Haug, B., Birchmeier, C., Role, L., Lai, C., Schwab, M.H., and Nave, K.A. (2004). Axonal neuregulin-1 regulates myelin sheath thickness. Science *304*, 700–703.

Miles, R., Tóth, K., Gulyás, A.I., Hájos, N., and Freund, T.F. (1996). Differences between somatic and dendritic inhibition in the hippocampus. Neuron *16*, 815–823.

Minichiello, L., Korte, M., Wolfer, D., Kühn, R., Unsicker, K., Cestari, V., Rossi-Arnaud, C., Lipp, H.P., Bonhoeffer, T., and Klein, R. (1999). Essential role for TrkB receptors in hippocampus-mediated learning. Neuron *24*, 401–414.

Mizoguchi, A., Ueda, T., Ikeda, K., Shiku, H., Mizoguti, H., and Takai, Y. (1989). Localization and subcellular distribution of cellular ras gene products in rat brain. Brain Res. Mol. Brain Res. *5*, 31–44.

Mizuno, K. (2013). Signaling mechanisms and functional roles of cofilin phosphorylation and dephosphorylation. Cell. Signal. *25*, 457–469.

Natt, O., Watanabe, T., Boretius, S., Radulovic, J., Frahm, J., and Michaelis, T. (2002). High-resolution 3D MRI of mouse brain reveals small cerebral structures in vivo. J. Neurosci. Methods *120*, 203–209.

Nave, K.A., and Salzer, J.L. (2006). Axonal regulation of myelination by neuregulin 1. Curr. Opin. Neurobiol. *16*, 492–500.

Neddens, J., and Buonanno, A. (2010). Selective populations of hippocampal interneurons express ErbB4 and their number and distribution is altered in ErbB4 knockout mice. Hippocampus *20*, 724–744.

Ozaki, M., Sasner, M., Yano, R., Lu, H.S., and Buonanno, A. (1997). Neuregulin-beta induces expression of an NMDA-receptor subunit. Nature *390*, 691–694.

Penzes, P., Cahill, M.E., Jones, K.A., VanLeeuwen, J.E., and Woolfrey, K.M. (2011). Dendritic spine pathology in neuropsychiatric disorders. Nat. Neurosci. *14*, 285–293.

Pitcher, G.M., Beggs, S., Woo, R.S., Mei, L., and Salter, M.W. (2008). ErbB4 is a suppressor of long-term potentiation in the adult hippocampus. Neuroreport *19*, 139–143.

Pitcher, G.M., Kalia, L.V., Ng, D., Goodfellow, N.M., Yee, K.T., Lambe, E.K., and Salter, M.W. (2011). Schizophrenia susceptibility pathway neuregulin 1-ErbB4 suppresses Src upregulation of NMDA receptors. Nat. Med. *17*, 470–478.

Role, L.W., and Talmage, D.A. (2007). Neurobiology: new order for thought disorders. Nature *448*, 263–265.

Shamir, A., Kwon, O.B., Karavanova, I., Vullhorst, D., Leiva-Salcedo, E., Janssen, M.J., and Buonanno, A. (2012). The importance of the NRG-1/ErbB4 pathway for synaptic plasticity and behaviors associated with psychiatric disorders. J. Neurosci. *32*, 2988–2997.

Stefansson, H., Sigurdsson, E., Steinthorsdottir, V., Bjornsdottir, S., Sigmundsson, T., Ghosh, S., Brynjolfsson, J., Gunnarsdottir, S., Ivarsson, O., Chou, T.T., et al. (2002). Neuregulin 1 and susceptibility to schizophrenia. Am. J. Hum. Genet. *71*, 877–892.

Tan, G.H., Liu, Y.Y., Hu, X.L., Yin, D.M., Mei, L., and Xiong, Z.Q. (2012). Neuregulin 1 represses limbic epileptogenesis through ErbB4 in parvalbumin-expressing interneurons. Nat. Neurosci. *15*, 258–266.

Ting, A.K., Chen, Y., Wen, L., Yin, D.M., Shen, C., Tao, Y., Liu, X., Xiong, W.C., and Mei, L. (2011). Neuregulin 1 promotes excitatory synapse development and function in GABAergic interneurons. J. Neurosci. *31*, 15–25.

Trommald, M., Hulleberg, G., and Andersen, P. (1996). Long-term potentiation is associated with new excitatory spine synapses on rat dentate granule cells. Learn. Mem. *3*, 218–228.

Uhlhaas, P.J., and Singer, W. (2010). Abnormal neural oscillations and synchrony in schizophrenia. Nat. Rev. Neurosci. *11*, 100–113.

Velanac, V., Unterbarnscheidt, T., Hinrichs, W., Gummert, M.N., Fischer, T.M., Rossner, M.J., Trimarco, A., Brivio, V., Taveggia, C., Willem, M., et al. (2012). Bace1 processing of NRG1 type III produces a myelin-inducing signal but is not essential for the stimulation of myelination. Glia *60*, 203–217.

Wang, J.Y., Frenzel, K.E., Wen, D., and Falls, D.L. (1998). Transmembrane neuregulins interact with LIM kinase 1, a cytoplasmic protein kinase implicated in development of visuospatial cognition. J. Biol. Chem. *273*, 20525–20534.

Weickert, C.S., Tiwari, Y., Schofield, P.R., Mowry, B.J., and Fullerton, J.M. (2012). Schizophrenia-associated HapICE haplotype is associated with increased NRG1 type III expression and high nucleotide diversity. Transl. Psychiatr. *2*, e104.

Wen, L., Lu, Y.S., Zhu, X.H., Li, X.M., Woo, R.S., Chen, Y.J., Yin, D.M., Lai, C., Terry, A.V., Jr., Vazdarjanova, A., et al. (2010). Neuregulin 1 regulates pyramidal neuron activity via ErbB4 in parvalbumin-positive interneurons. Proc. Natl. Acad. Sci. USA *107*, 1211–1216.

Woo, R.S., Li, X.M., Tao, Y., Carpenter-Hyland, E., Huang, Y.Z., Weber, J., Neiswender, H., Dong, X.P., Wu, J., Gassmann, M., et al. (2007). Neuregulin-1 enhances depolarization-induced GABA release. Neuron *54*, 599–610.

Yin, D.M., Chen, Y.J., Lu, Y.S., Bean, J.C., Sathyamurthy, A., Shen, C., Liu, X., Lin, T.W., Smith, C.A., Xiong, W.C., and Mei, L. (2013a). Reversal of behavioral deficits and synaptic dysfunction in mice overexpressing neuregulin 1. Neuron *78*, 644–657.

Yin, D.M., Sun, X.D., Bean, J.C., Lin, T.W., Sathyamurthy, A., Xiong, W.C., Gao, T.M., Chen, Y.J., and Mei, L. (2013b). Regulation of spine formation by ErbB4 in PV-positive interneurons. J. Neurosci. *33*, 19295–19303.

Zhong, C., Du, C., Hancock, M., Mertz, M., Talmage, D.A., and Role, L.W. (2008). Presynaptic type III neuregulin 1 is required for sustained enhancement of hippocampal transmission by nicotine and for axonal targeting of alpha7 nicotinic acetylcholine receptors. J. Neurosci. *28*, 9111–9116.

Cell Reports, Volume *8*

Supplemental Information

Dysregulated Expression of Neuregulin-1 by Cortical Pyramidal Neurons Disrupts Synaptic Plasticity

Amit Agarwal, Mingyue Zhang, Irina Trembak-Duff, Tilmann Unterbarnscheidt, Konstantin Radyushkin, Payam Dibaj, Daniel Martins de Souza, Susann Boretius, Magdalena M. Brzózka, Heinz Steffens, Sebastian Berning, Zenghui Teng, Maike Gummert, Martesa Tantra, Peter C. Guest, Katrin I. Willig, Jens Frahm, Stefan W. Hell, Sabine Bahn, Moritz J. Rossner, Klaus-Armin Nave, Hannelore Ehrenreich, Weiqi Zhang, and Markus H. Schwab

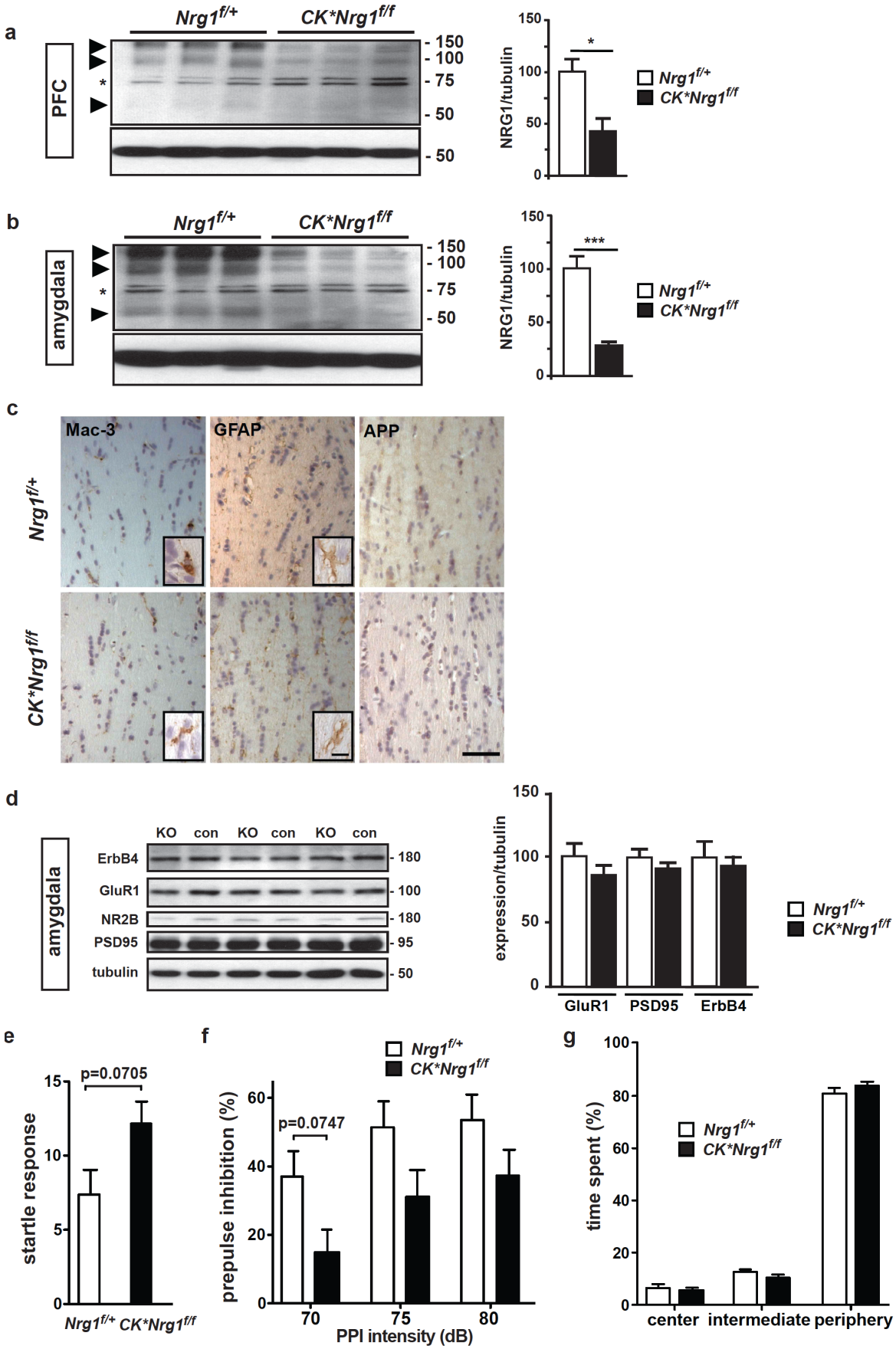
a
Nrg1f/+
CK*Nrg1f/f
PFC
150
100
75
50
50
NRG1/tubulin
*
b
amygdala
***
c
Mac-3
GFAP
APP
Nrg1f/+
CK*Nrg1f/f
d
KO con KO con KO con
ErbB4
GluR1
NR2B
PSD95
tubulin
180
100
180
95
50
expression/tubulin
GluR1
PSD95
ErbB4
e
p=0.0705
startle response
f
p=0.0747
prepulse inhibition (%)
PPI intensity (dB)
70
75
80
g
time spent (%)
center
intermediate
periphery

Supplemental Figures

Figure S1 (related to Figure 1):
Synaptic protein expression in *CK*Nrg1$^{f/f}$* mutants

(a) (left panel) Western blot analysis of protein lysates from prefrontal cortex (PFC) of *CK*Nrg1$^{f/f}$* mutants and *Nrg1$^{f/+}$* controls (age 15 months). Full-length CRD-NRG1 (~140 kDa) and Ig-NRG1 (~95 kDa) isoforms, and a C-terminal processing product (~60 kDa) were reduced in *CK*Nrg1$^{f/f}$* mutants (arrowheads). Asterisk indicates unspecific protein bands. **(right panel)** Densitometric quantification of NRG1 isoforms (140, 95 kDa). 'Integrated density' values were normalized to β-tubulin and are expressed as mean values. (n=3 per genotype; error bars, s.e.m.; *P<0.05; non-parametric, Mann-Whitney U, two-tailed t-test).

(b) (left panel) Western blot analysis of protein lysates from the amygdala (amy) of *CK*Nrg1$^{f/f}$* mutants and *Nrg1$^{f/+}$* controls. **(right panel)** Densitometric quantification of NRG1 isoforms (140; 95; and 60 kDa) as described for PFC. ***P<0.0001. Asterisk indicates unspecific protein bands.

(c) Immunostaining of the corpus callosum for markers of neuroinflammation (Mac3, activated microglia; GFAP, astrogliosis) and neurodegenration (APP, axonal swellings) on coronal brain sections from *CK*Nrg1$^{f/f}$* mutants and *Nrg1$^{f/+}$* controls (age 12 months). Sections were counterstained with hematoxylin. Scale bars, 50 µm; 10 µm (insets).

(d) (left panel) Western blot analysis of protein extracts from the amygdala of *CK*Nrg1$^{f/f}$* mutants and *Nrg1$^{f/+}$* controls after treatment with MK-801 (age 15 months). **(right panel)** Densitometric quantification as in (a).

(e, f) *CK*Nrg1$^{f/f}$* mice at 3-4 months show a tendency for an increased startle response (p=0.0705, Mann-Whitney U-test) and decreased pre-pulse inhibition of the startle response at 70 dB (effect of genotype $F_{1\text{-}44}$=3.5, p=0.0747, 2-way ANOVA for repeated measures).

(g) The fraction of time *CK*Nrg1$^{f/f}$* mutants spent in different zones of the open-field arena was similar for *CK*Nrg1$^{f/f}$* mutants and *Nrg1$^{f/+}$* controls.

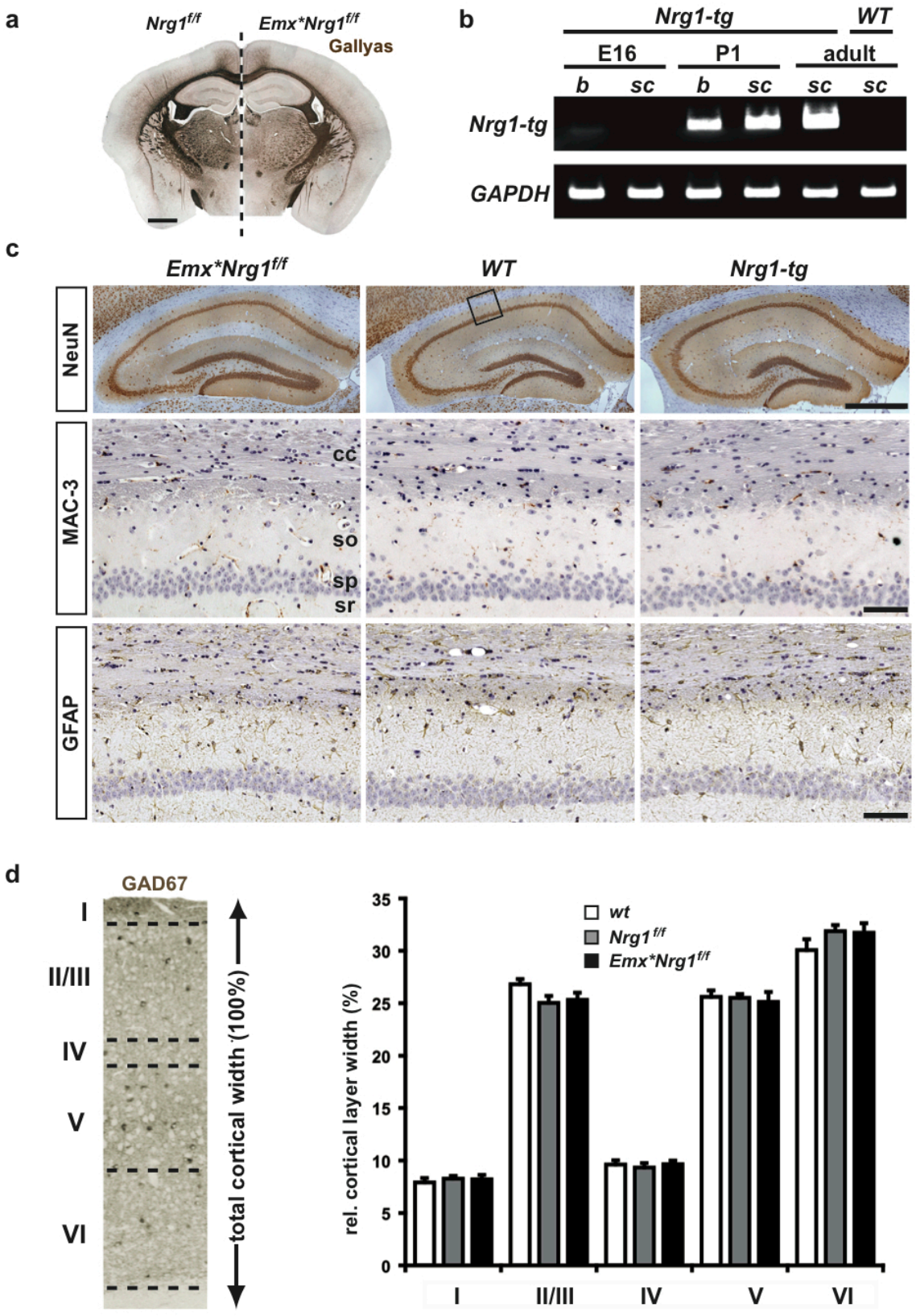
a
Nrg1f/f
Emx*Nrg1f/f
Gallyas
b
Nrg1-tg
WT
E16
P1
adult
b
sc
b
sc
sc
sc
Nrg1-tg
GAPDH
c
Emx*Nrg1f/f
WT
Nrg1-tg
NeuN
MAC-3
GFAP
cc
so
sp
sr
d
GAD67
I
II/III
IV
V
VI
total cortical width (100%)
rel. cortical layer width (%)
wt
Nrg1f/f
Emx*Nrg1f/f
0
5
10
15
20
25
30
35
I
II/III
IV
V
VI

Figure S2 (related to Figure 3):

Histology of *Emx*Nrg1*$^{f/f}$ mutants and *Nrg1-tg* mice

(a) Normal white matter structures and subcortical axonal projections in *Emx*Nrg1*$^{f/f}$ mutants compared to *Nrg1*$^{f/f}$ controls. Myelin staining (Gallyas silver impregnation) of coronal brain sections (age 3 months). Scale bar, 1mm.

(b) Onset of transgene expression in *Nrg1-tg* mice during late embryonic stages. RT-PCR with transgene-specific primers on brain (b) and spinal cord (sc) cDNA prepared from *Nrg1-tg* mice and *WT* at indicated stages. Note weak transgene expression in E16 brain. Amplification of GAPDH was used as an internal control.

(c) No signs of neurodegeneration and neuroinflammation in the hippocampus of *Emx*Nrg1*$^{f/f}$ mutants and *Nrg1-tg* mice. Immunostaining for neurons (NeuN) and markers of neuroinflammation (Mac3, activated microglia; GFAP, astrogliosis; higher magnification of CA1 region boxed in *WT* NeuN staining) on coronal brain sections from *Emx*Nrg1*$^{f/f}$ mutants, *Nrg1-tg* mice and *WT* (age 12 months). Abbreviations: cc, corpus callosum; so, stratum oriens; sp, stratum pyramidale; sr, stratum radiatum. Scale bars, 500 µm (top); 150 µm (middle and bottom).

(d) Normal cortical lamination in *Emx-Nrg1*$^{f/f}$ mutants and *Nrg1-tg* mice. Relative cortical layer width was determined based on GAD67 immunoreactivity on coronal brain sections (left panel, representative micrograph from *Nrg1*$^{f/f}$ mice, bregma -1.7; n=6 per genotype).

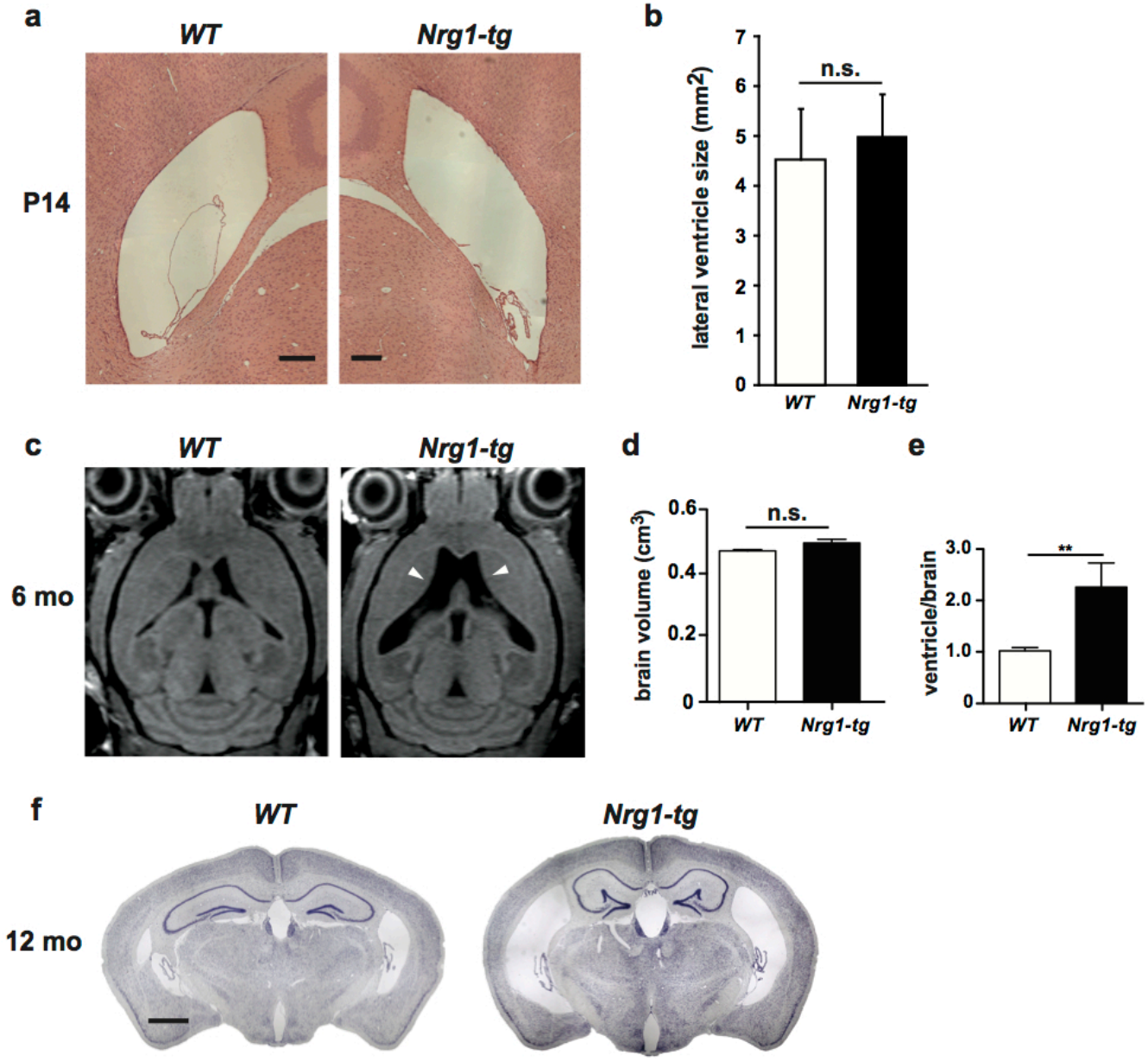
a
WT
Nrg1-tg
P14
b
lateral ventricle size (mm2)
n.s.
WT
Nrg1-tg
c
WT
Nrg1-tg
6 mo
d
brain volume (cm3)
n.s.
WT
Nrg1-tg
e
ventricle/brain
**
WT
Nrg1-tg
f
WT
Nrg1-tg
12 mo

Figure S3 (related to Figure 4):
Ventricular enlargement in adult *Nrg1-tg* mice

(a) Hematoxylin and Eosin staining of coronal brain sections (bregma -1.7) of *WT* and *Nrg1-tg* mice at P14. Scale bar, 200 μm.

(b) Lateral ventricles were not increased in *Nrg1-tg* compared to *WT* mice at P14. Ventricular size (bregma -1.7) was quantified on microscopic pictures (10x) using ImageJ (n=6 per genotype; error bars, s.e.m.; P=0.6991; non-parametric two-tailed t-test; ns, not significant).

(c) Enlarged lateral ventricles (white arrowheads) in *Nrg1-tg* compared to *WT* mice at 6 months (T1-weighted *in vivo* MRI).

(d) Volumetric analysis shows normal total brain volume (cm^3) in *Nrg1-tg* mice compared to *WT* (age 6 months; n=6 per genotype; error bars, s.e.m.; P=0.31; non-parametric two-tailed t-test; ns, not significant).

(e) Ventricular volume (percentage of total brain volume**)** is increased in *Nrg1-tg* mice compared to *WT*. *(n=5*, *WT*; n=4, *Nrg1-tg* mice; error bars, s.e.m.; **P<0.01; non-parametric two-tailed t-test).

(**f**) Enlarged lateral ventricles in *Nrg1-tg* mice at 12 months (Nissl staining of coronal brain sections). Note that ventricular enlargement results in deformation of the hippocampus. Scale bar, 1 mm.

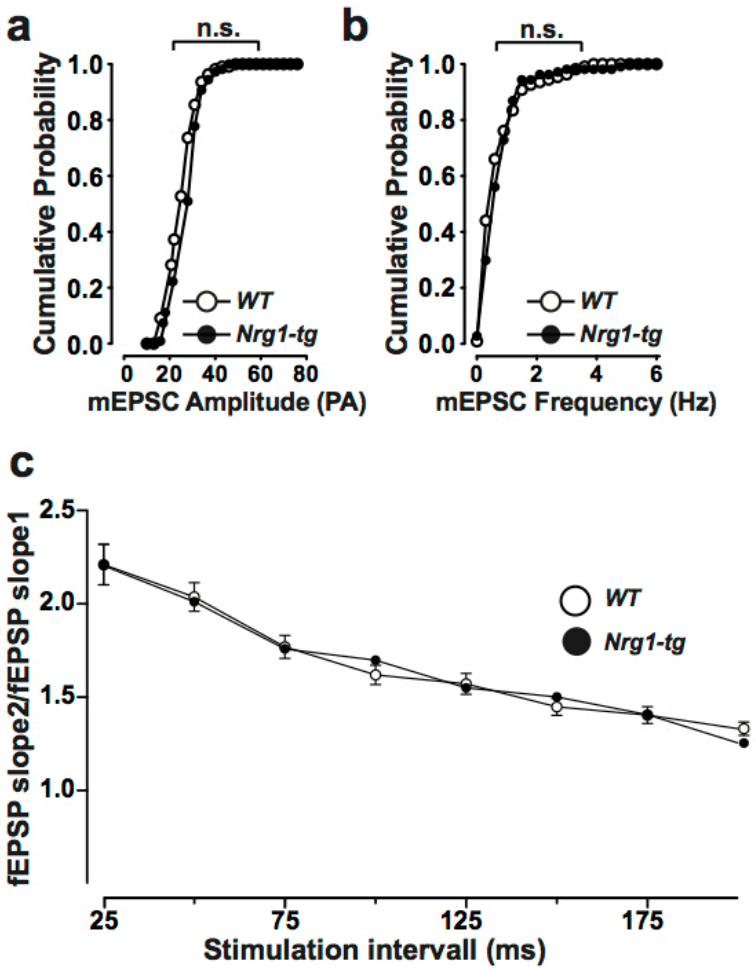

Figure S4 (related to Figure 5):

Elevated CRD-NRG1 expression has no effect on basal synaptic transmission and mEPSCs in CA1 pyramidal neurons

(a, b) Averaged mEPSC amplitude (a) and frequency (b) in pyramidal neurons from *Nrg1-tg* mice (n=15) were not changed compared to WT (n=10).

(c) Paired-pulse ratio at inter-stimulus intervals of 25–75 ms was unchanged in *Nrg1-tg* mice compared to WT.

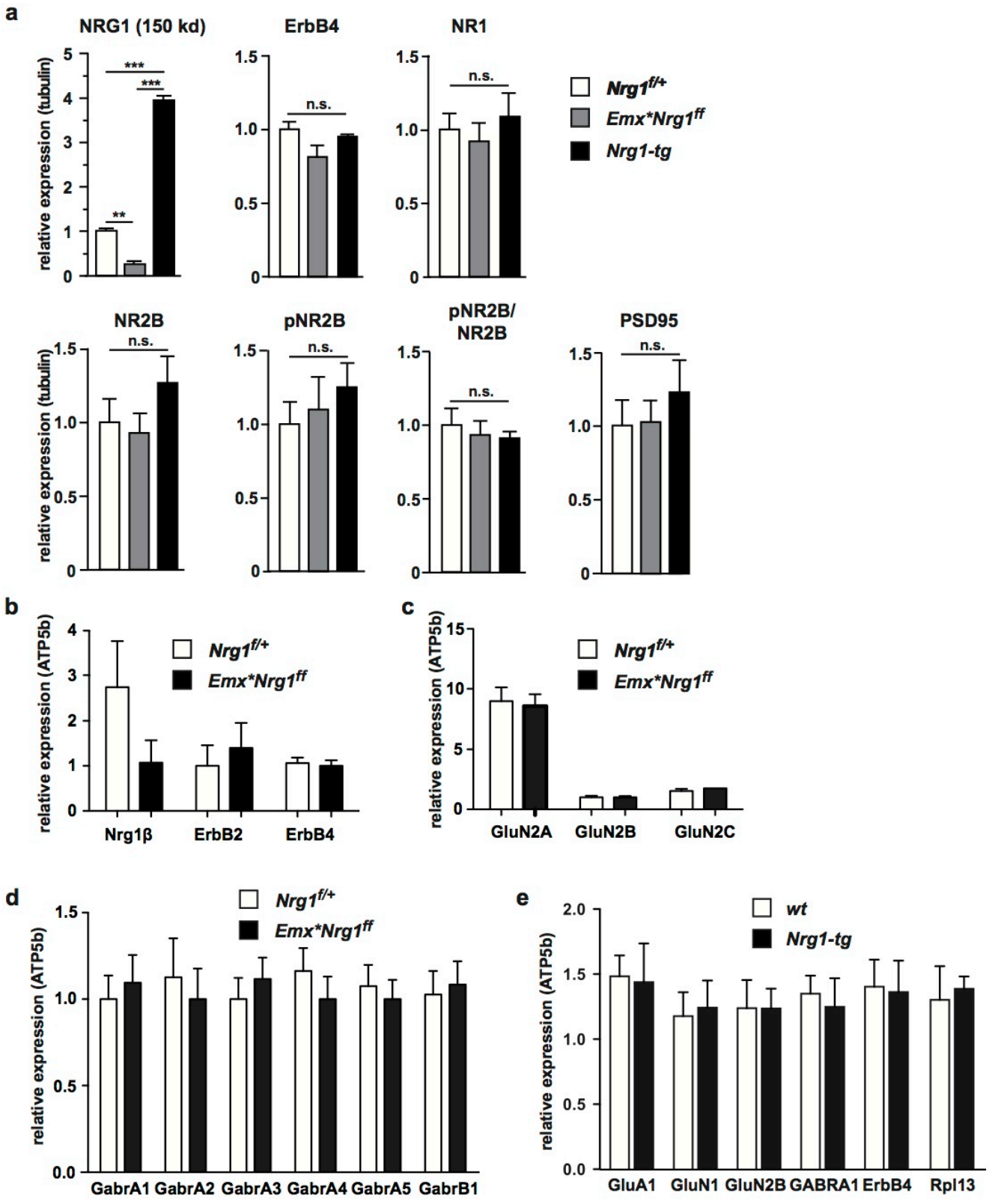
a
NRG1 (150 kd)
ErbB4
NR1
relative expression (tubulin)
***
***
**
n.s.
n.s.
Nrg1f/+
Emx*Nrg1ff
Nrg1-tg
NR2B
pNR2B
pNR2B/ NR2B
PSD95
b
relative expression (ATP5b)
Nrg1β
ErbB2
ErbB4
c
GluN2A
GluN2B
GluN2C
d
GabrA1
GabrA2
GabrA3
GabrA4
GabrA5
GabrB1
e
wt
GluA1
GluN1
GluN2B
GABRA1
ErbB4
Rpl13

Figure S5 (related to Figure 5):

Expression of neurotransmitter receptors in *Emx*Nrg1*$^{f/f}$ mutants and *Nrg1-tg* mice

(a) Densitometric quantification of proteins isolated from synaptic plasma membranes (TritonX-100 soluble and insoluble fractions) of *Emx*Nrg1*$^{f/f}$ mutants, *Nrg1-tg* mice, and *Nrg1*$^{f/+}$ controls. NRG1 was extracted from the TritonX-100 soluble fraction, all other proteins were solubilized in SDS-buffer from the postsynaptic density fraction. 'Integrated density' values were normalized to β-tubulin and expressed as mean values. (n=3 per genotype; error bars, s.e.m.; **P<0.01, ***P<0.001: one way ANOVA with post-hoc Tukey's multiple comparision test).

(b-d) Quantitative RT-PCR on pooled cDNA from the hippocampus of *Emx*Nrg1*$^{f/f}$ mutants (n=8) and controls (*Nrg1*$^{f/+}$, n=8) (age 4-5 months). **(a)** NRG1β expression was reduced by 70% in *Emx*Nrg1*$^{f/f}$ mutants (similar to NRG1 protein levels, see Fig. 3b), in contrast expression of ErbB2 and ErbB4 was not altered in *Emx*Nrg1*$^{f/f}$ mutants. **(b)** Expression of NMDA receptor 2 subunits A (GluN2A), B (GluN2B), C (GluN2C) and **(c)** all five subunits of GABAaα **(**GabrA1, GabrA2, GabrA3, GabrA4, GabrA5) and GABAaβ1 (GabrB1) receptors was unchanged in *Emx*Nrg1*$^{f/f}$ mutants compared to controls. Amplification of the housekeeping gene ATP5b was used for relative quantification.

(e) Quantitative RT-PCR on pooled cDNA from the hippocampus of *Nrg1-tg mice* (n=6) and wildtype mice (*WT,* n=6) (age 10-11 months). Expression of mRNAs for ionotropic glutamate receptors (AMPA receptor subunit 1, GluA1; NMDA receptor subunit 1, GluN1; subunit 2B, GluN2B), ionotropic GABA receptor (GABAa receptor α1; GABRA1) and ErbB4 receptor was similar in *Nrg1-tg* and *WT* mice. The housekeeping gene ribosomal protein L13 (Rpl13) was used as a quality control. Amplification of the housekeeping gene ATP5b was used for relative quantification.

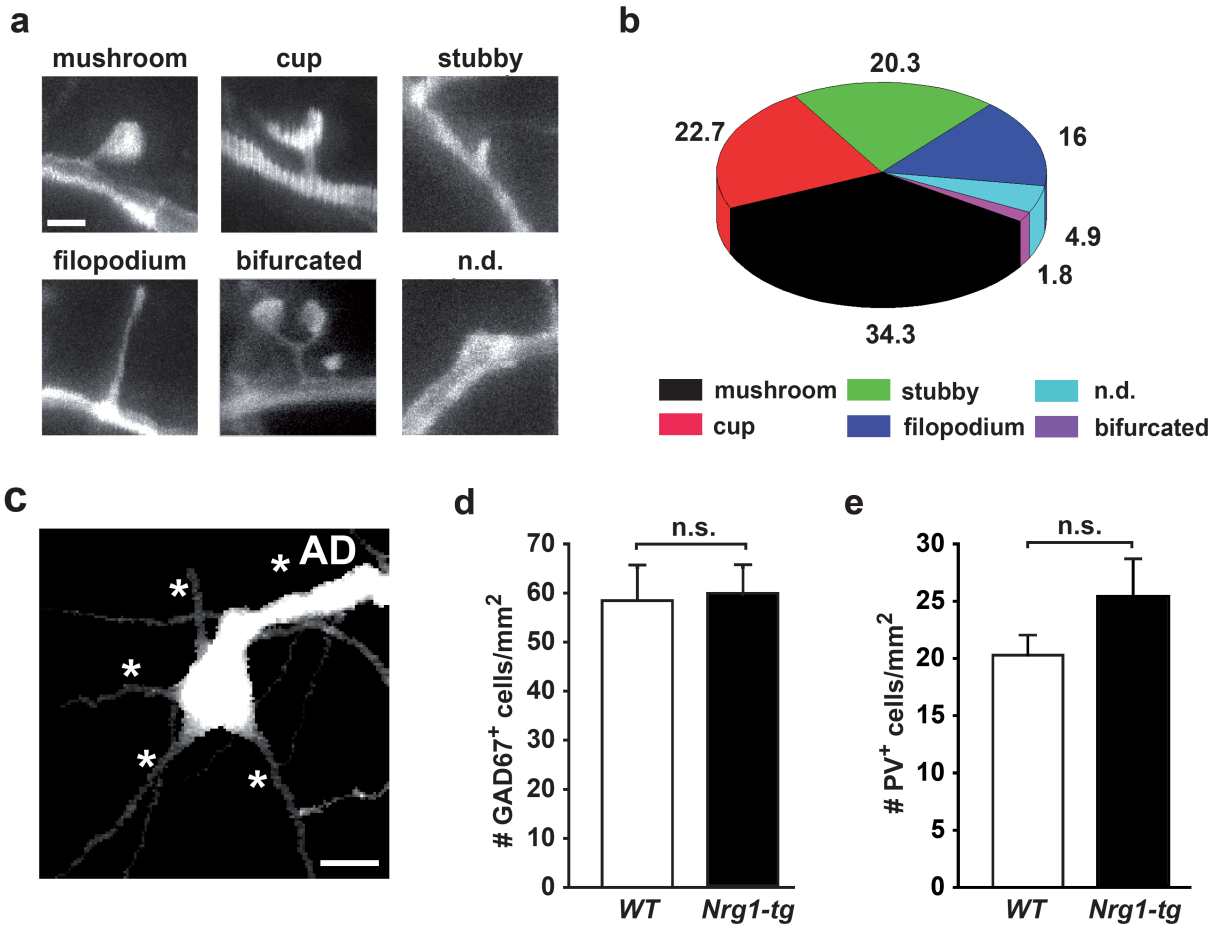

Figure S6 (related to Figure 6):

***In vivo* imaging of *CRD-Nrg1* transgenic mice**

(a) Representative examples of morphological spine classes in the MZ of 3 months old *Thy1.2-YFP* mice obtained by *in vivo* STED nanoscopy of dendrites derived from cortical layer V projection neurons. Scale bar, 1 µm.

(b) Frequency (in %) of spine classes in the MZ of *Thy1.2-YFP* mice (averaged values from n=4 mice, 30 dendrites/mouse; n.c., not classified).

(c) Primary dendrites (labeled by asterisks; AD, apical dendrite) emerging from layer V projection neuron marked by white box in Fig. 6a. Scalebar, 20 µm.

(d) Number of GAD67$^+$ interneurons in the hippocampus of *Nrg1-tg* mice and *WT* at P14 (Bregma, -1.7, both hemispheres; n=6 mice per genotype, n.s., not significant).

(e) Number of PV$^+$ interneurons in the hippocampus of *Nrg1-tg* mice and *WT* at P14 (Bregma, -1.7, both hemispheres; n=6 mice per genotype, n.s., not significant).

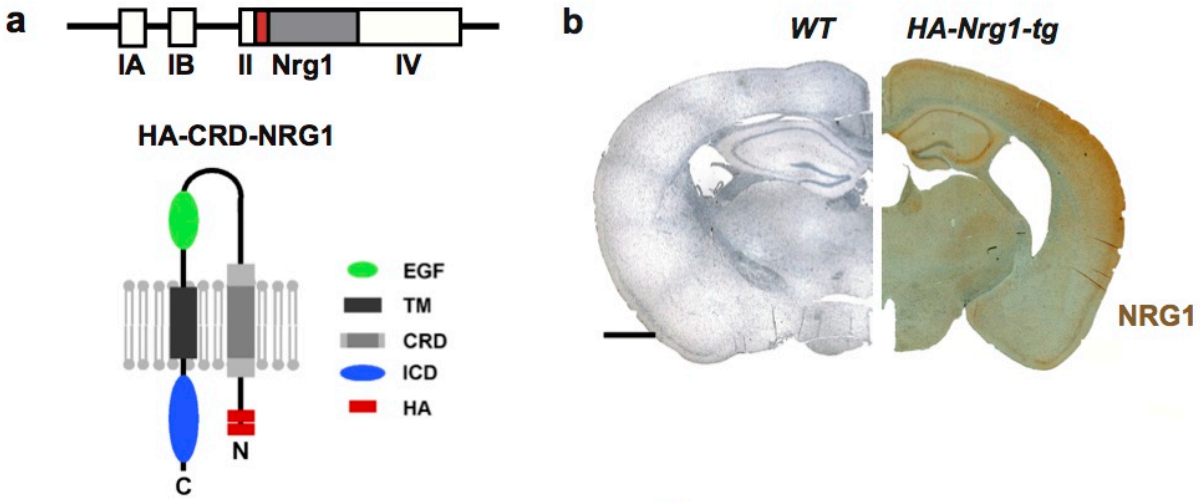
a
IA
IB
II
Nrg1
IV
HA-CRD-NRG1
EGF
TM
CRD
ICD
HA
N
C
b
WT
HA-Nrg1-tg
NRG1

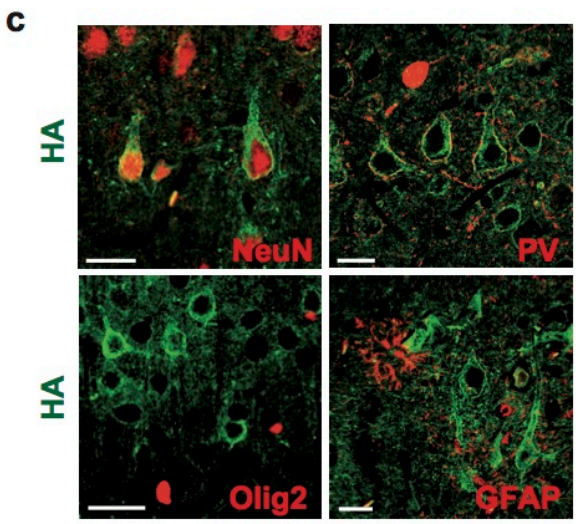
c
HA
NeuN
PV
HA
Olig2
GFAP

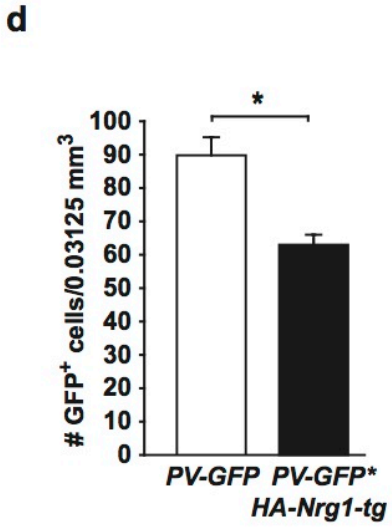
d
*
GFP+ cells/0.03125 mm3
100
90
80
70
60
50
40
30
20
10
0
PV-GFP
PV-GFP*
HA-Nrg1-tg

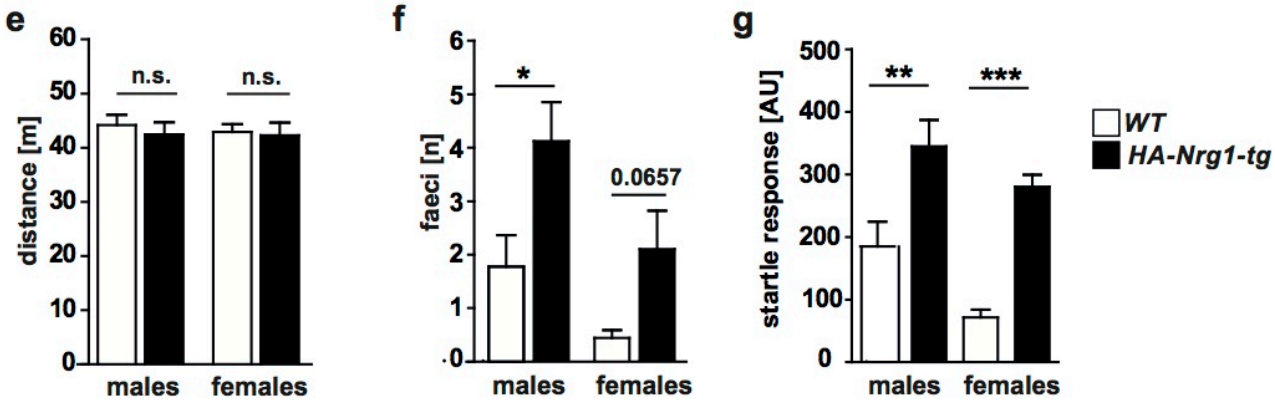
e
distance [m]
60
50
40
30
20
10
0
n.s.
n.s.
males
females
f
faeci [n]
6
5
4
3
2
1
0
*
0.0657
males
females
g
startle response [AU]
500
400
300
200
100
0
**
***
males
females
WT
HA-Nrg1-tg

Figure S7 (related to Figure 7):

Expression analysis and behavioral characterization of *HA-Nrg1-tg* mice

(a) (upper panel) Structure of the Thy1.2 transgene cassette (red box, HA epitope; grey box, full-length CRD-Nrg1 cDNA; white boxes, exons I-IV of the Thy1.2 gene). (lower panel) In HA-CRD-NRG1 two HA epitope tags are located at the N-terminus of CRD-NRG1. CRD, cystein-rich domain; EGF, epidermal growth factor-like domain; HA, HA epitope tag; ICD, intracellular domain; TM, transmembrane domain.

(b) Chromogenic NRG1 immunostaining (ICD domain) on coronal brain sections from wildtype (*WT*) and HA-CRD-NRG1 expressing transgenic mice (*HA-Nrg1-tg*) at 4 months of age. Note enlarged lateral ventricle in *HA-Nrg1-tg* brain, similar to *Nrg1-tg* mice. Scalebar, 1 mm.

(c) Fluorescent immunostaining for the HA epitope and cell type-specific markers (neurons, NeuN; interneurons, PV; oligodedrocytes, Olig2; astrocytes, GFAP) on coronal brain sections from *HA-Nrg1-tg* mice (age 4 months). Scalebars, 25 µm (PV, 20 µm).

(d) Number of GFP^+ interneurons in a cortical column of 250*250*500 µm (0.03125 mm^3) of *PV-GFP*HA-Nrg1-tg* mice (n=2) and *PV-GFP* controls (n=5) obtained by *in vivo* two-photon imaging (*P<0.05).

(e) Distance travelled in the open-field test was similar in *HA-Nrg1-tg* and *WT* mice of both sexes (age 2-3 months, males: p=0.5575, females p=0.6835; Mann-Whitney test).

(f) Male *HA-Nrg1-tg* mice showed more frequent defecation compared to *WT* mice during the open-field test (P=0.0129; Mann-Whitney test); a similar tendency (P=0.0657) was observed for female *HA-Nrg1-tg* mice.

(g) *HA-Nrg1-tg* mice (males: P=0.0083; females: P<0.0001; Mann-Whitney test) displayed increased startle response to a 120 dB pulse in the prepulse inhibition test. (*WT* mice: males, n=18; females, n=18; *HA-Nrg1-tg* mice: males, n=16; females, n=10. Error bars ± s.e.m. *P <0.05; **P<0.01; ***P<0.001; n.s., not significant; Mann-Whitney U-test. AU, arbitrary units).

Supplemental Tables

Biological Process	Gene	Accession	Protein Description	Molecular function	MW	Ratio	FC	ID Pep	Wilcoxon	t-test	q value
Cell comm. and signalling	Camk2a	KCC2A_MOUSE	Ca+2/calmodulin-dependent protein kinase type II alpha chain	Protein serine/threonine kinase activity	54115	0,67	-1,49	51	0,0304	0,0407	0,2665
	Camk2b	KCC2B_MOUSE	Ca+2/calmodulin-dependent protein kinase type II beta chain	Protein serine/threonine kinase activity	60461	0,77	-1,30	43	0,0304	0,0273	0,2665
	Eef1d	EF1D_MOUSE	Elongation factor 1-delta	Guanyl-nucleotide exchange factor activity	31293	0,81	-1,23	2	0,0141	0,0109	0,3952
	Gna14	GNA14_MOUSE	Guanine nucleotide-binding protein subunit alpha-14	GTPase activity	41528	0,90	-1,11	8	0,0304	0,0174	0,3952
	Hcls1	HCLS1_MOUSE	Hematopoietic lineage cell-specific protein	Molecular function unknown	54240	1,09	1,09	3	0,0141	0,0095	0,2665
	Mapk1	MK01_MOUSE	Mitogen-activated protein kinase 1	Protein serine/threonine kinase activity	41276	0,92	-1,08	33	0,0464	0,0449	0,3952
	Mrc1	MRC1_MOUSE	Macrophage mannose receptor 1	Receptor activity	164981	1,29	1,29	2	0,0194	0,0417	0,3952
	Omg	OMGP_MOUSE	Oligodendrocyte-myelin glycoprotein	Cell adhesion molecule activity	49284	0,79	-1,26	5	0,0073	0,0155	0,2665
	Phb	PHB_MOUSE	Prohibitin	Receptor signaling complex scaffold activity	29820	0,89	-1,12	35	0,0404	0,0345	0,3952
	Pld2	PLD2_MOUSE	Phospholipase D2	Phospholipase activity	106168	1,43	1,43	2	0,0304	0,0465	0,3952
	Ppp3cc	PP2BC_MOUSE	Ser/Thr-protein phosphatase 2B catalytic subunit gamma	Protein serine/threonine phosphatase activity	58699	1,23	1,23	6	0,0141	0,0057	0,3952
	Rab8a	RAB8A_MOUSE	Ras-related protein Rab-8A	GTPase activity	23668	1,19	1,19	16	0,0404	0,0291	0,3952
	Sh3gl2	SH3G2_MOUSE	Endophilin-A1	Molecular function unknown	39955	0,87	-1,15	6	0,0464	0,0323	0,2665
	Stip1	STIP1_MOUSE	Stress-induced-phosphoprotein 1	Receptor signaling complex scaffold activity	62582	0,72	-1,40	2	0,0351	0,0199	0,3952
Cell growth/maintenance	Actr1b	ACTY_MOUSE	Beta-centractin	Structural constituent of cytoskeleton	42281	0,90	-1,11	2	0,0464	0,0346	0,2665
	Dctn2	DCTN2_MOUSE	Dynactin subunit 2	Motor activity	44117	0,77	-1,30	3	0,0102	0,0042	0,2665
	Map1a	MAP1A_MOUSE	Microtubule-associated protein 1A	Cytoskeletal protein binding	30014	1,10	1,10	37	0,0304	0,0406	0,3952
	Tnr	TENR_MOUSE	Tenascin-R	Extracellular matrix structural constituent	149589	0,91	-1,10	86	0,0120	0,0045	0,2665
	Vcan	CSPG2_MOUSE	Versican core protein	Extracellular matrix structural constituent	366787	0,80	-1,25	2	0,0043	0,0012	0,2665
	Actr2	ARP2_MOUSE	Actin-related protein 2	Structural constituent of cytoskeleton	44761	0,89	-1,13	23	0,0464	0,0429	0,3952
Immune response	Mog	MOG_MOUSE	Myelin-oligodendrocyte glycoprotein	Antigen binding	28271	0,78	-1,29	13	0,0061	0,0050	0,3952
Energy Metabolism	Ak4	KAD4_MOUSE	Adenylate kinase isoenzyme 4, mitochondrial	Catalytic activity	25062	0,84	-1,19	7	0,0226	0,0175	0,3952
	Ahcyl1	SAHH2_MOUSE	Putative adenosylhomocysteinase 2	Hydrolase activity	58951	0,71	-1,42	4	0,0120	0,0135	0,3952
	Apeh	APEH_MOUSE	Acylamino-acid-releasing enzyme	Hydrolase activity	81522	1,22	1,22	3	0,0351	0,0203	0,2665
	Gpi	G6PI_MOUSE	Glucose-6-phosphate isomerase	Isomerase activity	62767	0,73	-1,37	86	0,0262	0,0464	0,2665
	Phka1	KPB1_MOUSE	Phosphorylase b kinase regulatory subunit alpha	Phosphorylase activity	138825	0,70	-1,43	2	0,0194	0,0347	0,2665
	Prdx3	PRDX3_MOUSE	Thioredoxin-dependent peroxide reductase, mitochondrial	Peroxidase activity	28127	1,14	1,14	12	0,0194	0,0393	0,3952
	Psat1	SERC_MOUSE	Phosphoserine aminotransferase	Transaminase activity	40473	0,78	-1,28	14	0,0226	0,0245	0,3952
	Qdpr	DHPR_MOUSE	Dihydropteridine reductase	Catalytic activity	25570	0,78	-1,28	19	0,0304	0,0269	0,3952
	Tecr	GPSN2_MOUSE	Synaptic glycoprotein SC2	Catalytic activity	36090	0,87	-1,15	2	0,0464	0,0389	0,2665
Regulation of cell cycle	Eef1a1	EF1A1_MOUSE	Elongation factor 1-alpha 1	Transcription regulator activity	50114	0,62	-1,61	29	0,0166	0,0321	0,2665
Reg. of nucleic acid metab.	Aco1	ACOC_MOUSE	Cytoplasmic aconitate hydratase	Isomerase activity	98126	1,16	1,16	4	0,0141	0,0163	0,3952
	Ddx5	DDX5_MOUSE	Probable ATP-dependent RNA helicase DDX5	RNA binding	69290	1,13	1,13	5	0,0194	0,0083	0,2665
	Lrpprc	LPPRC_MOUSE	Leucine-rich PPR motif-containing protein, mitochondrial	RNA binding	156615	1,11	1,11	7	0,0464	0,0362	0,2665
	Prpsap2	KPRB_MOUSE	Phosphoribosyl pyrophosphate synthetase-associated protein 2	Molecular function unknown	40881	0,81	-1,23	5	0,0073	0,0026	0,3952
Transport	Atp1b1	AT1B1_MOUSE	Sodium/potassium-transporting ATPase subunit beta-1	ATPase activity	35195	0,80	-1,25	31	0,0226	0,0186	0,2665
	Pacs1	PACS1_MOUSE	Phosphofurin acidic cluster sorting protein 1	Receptor signaling complex scaffold activity	104829	1,13	1,13	3	0,0404	0,0314	0,2665
	Slc12a6	S12A6_MOUSE	Solute carrier family 12 member 6	Auxiliary transport protein activity	127527	1,15	1,15	19	0,0120	0,014	0,2665
	Slc4a10	S4A10_MOUSE	Sodium-driven chloride bicarbonate exchanger	Auxiliary transport protein activity	125817	1,27	1,27	8	0,0262	0,0373	0,2665
Unknown	Sept6	SEPT6_MOUSE	Septin-6;	Molecular function unknown	49620	0,86	-1,17	2	0,0464	0,0386	0,2665

Table S1 (related to Figure 5):

Differentially expressed proteins in the hippocampus of *Nrg1-tg* mice

Proteins with differential expression between *Nrg1-tg* and *WT* mice were identified by LC-MSE as described in the methods section. Indicated are the biological processes, gene names (gene), UniProt accession codes, protein description, molecular function, molecular weight (MW), ratio (*Nrg1-tg*/*WT*), number of peptides identified (ID pep), Wilcoxin, t-test and q-values for each protein.

Gene name	Accession	Protein description
GRIN1	Q05586	Glutamate [NMDA] receptor subunit zeta-1
GRIN2B	Q13224	Glutamate [NMDA] receptor subunit epsilon-2
GRIN2A	Q12879	Glutamate [NMDA] receptor subunit epsilon-1
GRIK2	Q13002	Glutamate receptor, ionotropic kainate 2
GRIA1	P42261	Glutamate receptor AMPA 1
ITPR1	Q14643	Inositol 1,4,5-trisphosphate receptor type 1
AHCYL1	Q2NKW8	Adenosylhomocysteinase
NOS1	P29475	Nitric oxide synthase, brain
RARA	P10276	Retinoic acid receptor alpha
FMR1	Q06787	Fragile X mental retardation protein 1
HTT	P42858	Huntingtin
NSF	P46459	Vesicle-fusing ATPase
DLG1	Q12959	Disks large homolog 1
DLG2	Q15700	Disks large homolog 2
DLG4	P78352	Disks large homolog 4
ATP5B	P06576	ATP synthase subunit beta, mitochondrial
SNAP25	P60880	Synaptosomal-associated protein 25
STX1A	Q16623	Syntaxin-1A
STXBP1	P61764	Syntaxin-binding protein 1
KCNA2	P16389	Potassium voltage-gated channel subfamily A member 2
VCAM1	P19320	Vascular cell adhesion molecule 1
IL6	IP05231	Interleukin-6
APP	P05067	Amyloid beta A4 protein

Table S2 (related to Figure 5):

"Interactom" of differentially expressed proteins in *Nrg1-tg* mice

List of proteins in the IPKB database known to interact with the uploaded proteins from Table S1. The table gives the gene name, accession code and protein description.

Table S3: Summary of "endophenotypes" in transgenic mice overexpressing various *neuregulin1* isoforms.

Endophenotype	Full-length CRD-NRG1 [a]	Full-length Ig-NRG1 [b]	Full-length Ig-NRG1 [c]	BACE1-processed Ig-NRG1 [d]
interneuron migration/numbers	Reduced PV+ interneurons	*nd*	unchanged	*nd*
spines	abnormal growth	*nd*	*nd*	*nd*
LTP	reduced	unchanged	*nd*	*nd*
glutamatergic neurotransmission[1]	unchanged	unchanged[2]	reduced EPSC frequency	*nd*
GABAergic neurotransmission[1]	increased IPSC frequency	reduced γ- oscillation	reduced IPSC amplitude	*nd*
ventricular size	increased	unchanged[3]	*nd*	*nd*
motor activity (open field)	unchanged	increased	increased	increased
PPI	reduced	*nd*	reduced	unchanged

[a]current study, **[b]Deakin et al., 2011**, **[c]Yin et al., 2013**, **[d]Luo et al., 2013**

[1]glutamatergic projection neurons, [2]paired pulse facilitation, [3]personal communication, nd: not determined

Table S4: Summary of "endophenotypes" in NRG1

mouse mutants of various *neuregulin1* isoforms.

Endophenotype	*CamKII*Nrg1*$^{f/f}$ [a]	*CRD-Nrg1*$^{+/-}$ [b]	*Ig-Nrg1*$^{+/-}$ [c]	*Nrg1*$^{+/-}$ [d]
interneuron migration/numbers	unchanged	*nd*	*nd*	*nd*
spines	*nd*	reduced spine density	*nd*	*nd*
LTP	reduced	reduced[2]	*nd*	increased
glutamatergic neurotransmission	reduced mEPSC (amplitude only)	mEPSC unchanged[3]	*nd*	*nd*
GABAergic neurotransmission	increased mIPSC (amplitude only)[1]	*nd*	*nd*	*nd*
ventricular size	reduced	increased	*nd*	*nd*
motor activity (open field)	reduced	unchanged	unchanged	increased
PPI	reduced	reduced	unchanged	reduced

[a]current study, **[b]Chen et al., 2008; Jiang et al., 2013**, **[c]Rimer et al., 2005; Rao et al., 2004**, **[d]O'Tuathaigh et al., 2010; Stefansson et al., 2002**, **Gerlai et al., 2000; Shamir et al., 2012**.

[1]CA1 pyramidal neurons, [2]cortical–BLA synapses, [3]BLA pyramidal neurons

Supplemental Experimental Procedure.

Protein analysis. Protein lysates were prepared using an Ultraturrax (T8). Tissues were homogenized in 1 ml of modified RIPA buffer (50 mM Tris-HCl pH 7.4, 150 mM NaCl, 1 mM EDTA, 0.1% SDS, 1% TritonX-100, 1% Sodium deoxycholate, 1 mM PMSF and 1 mM Sodium vanadate) and protease inhibitors (Complete tablets, Roche). To study ErbB4 phosphorylation, protein lysates were prepared using sucrose lysis buffer (320 mM Sucrose, 10 mM Tris pH7,4, 1 mM $NaHCO_3$, 1 mM $MgCl_2$) complemented with Roche Protease Inhibitor complete plus mini and Roche PhoSTOP phosphatase inhibitor. For Western Blotting 1-5 µg [50 µg, for NRG1] of cortical or total brain lysate was size-separated on 8% SDS-polyacrylamide gels and blotted onto PVDF membranes (Hybond™-P) following instructions from Invitrogen. Membranes were blocked in 5% milk powder prepared in TBS buffer (50 mM Tris-HCl, pH 7.4 and 150 mM NaCl) for 1-2 hours at room temperature. Primary antibodies directed against GluR1 (pRb, 1:1000, Chemicon), NMDAR1 (mM, 1:7000, Synaptic systems), NMDAR2B (pRb, 1:2000, Chemicon), pErbB4 (mM, 1:1000, Cell Signaling), NRG1 (Sc-348, pRb, 1:500, Santa Cruz Biotechnology), nAchα7 (mM, 1:1000, Covance), PSD95 (mM, 1:10000, Upstate), β-actin (mM, 1:1000, Millipore) and tubulin (mM, 1:2000, Sigma) were diluted in blocking buffer and incubated overnight at 4°C. Membranes were washed three times (10 min each) in TBS-T buffer (50 mM Tris-HCl, pH 7.4, 150 mM NaCl and 0.05% Tween-20), followed by an incubation with a horseradish peroxidase-conjugated secondary antibody (diluted 1:5,000-10,000 in blocking buffer). After 5 additional wash steps (10 min each) with TBS-T buffer, proteins were detected with an enhanced chemiluminescence kit (Western Lightning™, Western Blot Chemiluminescence Reagent Plus, PerkinElmer Life Sciences, Inc.) according to the manufacturer's instructions. Exposure of ECL films (Hyperfilm™, Amersham Biosciences) was carried out varying from 10 seconds to 15 minutes depending upon signal intensity. Films were scanned. The densitometric analysis of scanned ECL films was carried out using ImageJ (NIH). The peak intensity value for the band of interest calculated by ImageJ was normalized to the peak intensity value of tubulin. The normalized values (±SEM) were depicted as histograms using GraphPad Prism 5.0.

Synaptosomes and synaptic plasma membrane preparation. The protocol used in this study involves the preparation of isolated nerve terminals (synaptosomes) by a sucrose density gradient technique **(Dodd et al., 1981)**. We modified this technique to rapidly isolate synaptosomes from very small quantities of starting material (such as cerebral cortices and hippocampi microdissected from two mouse brains). Synaptosomes isolated by this technique were lysed in Tris-HCl buffer (pH 8.0) to obtain crude synaptic plasma membranes (SPM), which were fractionated into Triton X-100 soluble and insoluble fraction by ultra-centrifugation **(Mizoguchi et al., 1989)**. The detailed steps for the preparation of crude synaptosomal membrane are as follows. Mice were sacrificed by cervical spinal cord dislocation and were decapitated. Brains were instantly removed and were micro dissected in chilled 1X Phosphate buffered saline (PBS) to isolate forebrain by cutting out olfactory bulb, midbrain, hindbrain and cerebellum. Each dissected forebrain was further separated into cerebral cortex and hippocampus, which were independently prepared for synaptosomal isolation. Cerebral cortices obtained from two mice were placed into a glass potter containing 1.5 ml of homogenization buffer (0.32 mM Sucrose in 4 mM HEPES buffer at pH 7.3) and was gently homogenized using a glass-Teflon homogenizer (16 up/down strokes, 900 rpm). The pistil was further rinsed with 1.5 ml of homogenization buffer for complete recovery of homogenate. The homogenate was centrifuged at 1000_{gmax} for 10 min at 4ºC. The resulting pellet containing large cell fragments and nuclei was discarded and the supernatant was collected. The supernatant (0.32 M) was gently placed on the 0.8 M layer of the sucrose gradient that was prepared by layering 3.0 ml sucrose solutions of following concentrations: 1.2 M (lowermost), 1.0 M, 0.8 M. The resultant sucrose gradient was centrifuged at 110,000 $_{gmax}$ for 2 hours at 4ºC to separate brain lysates into various sub-cellular fractions. Relatively pure fraction of synaptosomes (~50% purity) was obtained from the interface between 1.0 M and 1.2 M sucrose. Further on synaptosomes were diluted in 3.5 ml of homogenization buffer and pelleted by centrifugation at 37,000 $_{gmax}$ for 20 min at 4ºC. The pelleted synaptosomes were lysed by osmotic shock in 1.8ml of 4 mM HEPES buffer (pH 7.4) and centrifuged at 37,000 $_{gmax}$ for 20 min at 4ºC

to get crude synaptic membranes (SPMs). SPMs were further fractionated into Triton X-100 buffer (6 mM Tris-HCl, 1.0% TritonX-100 (pH 8.0)) soluble and insoluble fraction by centrifugation at $135{,}000_{gmax}$ for 20 min at 4ºC. The supernatant (i.e. TritonX-100 soluble fraction) is solubilized synaptic membranes. TritonX-100 insoluble fraction (PSD fraction), mainly consisting of post-synaptic density proteins was solubilized using SDS buffer (2% Sodium dodecyl sulfate, 5% 2-mercaptoethanol in 50 mM Tris-HCl, pH 7.4). The composition of synaptic protein in TritonX-100 soluble and insoluble fractions were analysed using SDS-PAGE and by western blotting as described above, and following primary antibodies were used: ErbB4 (Sc-283, pRb, 1:1000, Santa Cruz Biotechnology), NMDAR1 (mM, 1:7000, Synaptic systems), NMDAR2B (pRb, 1:2000, Chemicon), phosphorylated NMDAR2B (pRb, 1:1000, Chemicon), NRG1 (Sc-348, pRb, 1:500, Santa Cruz Biotechnology), PSD95 (mM, 1:10000, Upstate) and tubulin (mM, 1:2000, Sigma).

Histology and immunostaining. Mice were anesthetized with avertin and perfused with 4% PFA in 0.1 M Phosphate buffer. Brains were postfixed in 4% PFA for one hour to overnight at 4°C. After post-fixation tissues were either embedded in paraplast or stored in 1% PFA in 0.1 M PBS at 4°C until further processed. Free-floating vibratome (40-50 µm) or paraffin sections (5 µm) were incubated overnight with primary antibodies directed against CNP (mM, 1:150, Sigma), GAD67 (mM, 1:1000, Chemicon), GFAP (pRb, 1:200, DAKO; mM, 1:500, Chemicon), HA epitope (mM, 1:250, Covance; pRb, 1:500, Abcam), MAP2 (mM, 1:1000, Sigma), NeuN, mM, 1:200, Chemicon), NRG1 (Sc-348, pRb, 1:500, Santa Cruz Biotechnology), Olig2 (pRb, 1:200, John Alberta, Harvard), PV (pRb, 1:200, Swant). Sections were further incubated with secondary antibodies Cy2 (1:10000, Jackson ImmunoResearch), Cy3 (1:10000, Jackson ImmunoResearch), Alex-488 and Alexa 555 (1:2000, Invitrogen) for 1 hour at room temperature. For the analysis of neurodegenerative changes and cell number analysis, 5-7 mm thick paraplast embedded brain sections were used. Tissue sections were stained with histological stains, such as Haematoxylin-Eosin (H&E, Merck) and Cresyl Violet (Nissl), or incubated with primary antibodies against GAD67 (mM, 1:1000, Chemicon), GFAP (pRb, 1:200, DAKO), Iba1 (pRb, 1:1000,

Wako), Mac3 (mRat, 1:400, Pharmingen), NeuN (mM, 1:100, Chemicon), NRG1 (Sc-348, pRb, 1:500, Santa Cruz Biotechnology) for DAB based immunostaining (Dako-$LSAB_2$ kit was used according to manufacturer's instructions). Digital images of stained sections were obtained using Zeiss 510-meta LSM (Zeiss, Germany), Axiophot (Zeiss, Germany), DMRXA (Leica, Germany) microscopes. All images were processed with Photoshop CS3, Illustrator CS3 software (Adobe), ImageJ [NIH, Bethesda, USA, (http://rsbweb.nih.gov/ij)] and Fiji (http://fiji.sc/wiki/index.php/Fiji).

Electrophysiology. For slice preparation, mice (10-12 weeks old) were deeply anesthetized with isofluran before decapitation. The brain was quickly removed and immersed for 2-3 min in ice-cold cutting solution (3 mM KCl, 1.25 mM NaH_2PO_4, 6 mM $MgSO_4$, 26 mM $NaHCO_3$, 0.2 mM $CaCl_2$, 10 mM Glucose, 218 mM Sucrose). Transverse slices (300 µm) were cut with a vibroslicer and transferred to recording chamber that was continuously perfused with artificial cerebrospinal fluid (ACSF; 126 mM NaCl, 3 mM KCl, 1.25 mM NaH_2PO_4, 1 mM $MgSO_4$, 26 mM $NaHCO_3$, 2 mM $CaCl_2$, 10 mM Glucose, aerated with 95% O_2 and 5% CO_2 (3-4 ml/min).

Field recording electrodes were pulled from thin-walled borosilicate glass capillaries and filled with ACSF. Extracellular field potential recordings were done using a custom built DC amplifier. Data were digitized by a DigiData 1322A (Molecular Devices, Sunnyvale, CA, USA). Initial data analysis was done in Clampfit 10.0 (Molecular Devices, Sunnyvale, CA, USA). The stimulation electrode was placed in stratum radiatum at the CA3/CA1 junction for the activation of Schaffer collaterals. The recording electrode was placed in the stratum radiatum of the CA1 region. The magnitude of fEPSPs was measured as amplitude (baseline to peak) and slope (20-80% level of the falling phase). Baseline fEPSCs were set to about 50% of maximum responses. LTP was induced by three trains separated by 20 s, each train consisting of 100 Hz stimulation for 1s. Post-train responses were measured every 20 s for 60 min. fEPSPs were filtered by a four-pole Bessel filter at a corner frequency of 2 kHz, and digitized at a sampling rate of 20 kHz using the DigiData 1400A interface (Molecular Devices, Sunnyvale, CA).

For whole-cell patch recordings, acute transverse hippocampal or cortical slices (300 µm) were prepared as described above. All recordings were performed in CA1 pyramidal neurons or cortical layer V projection neurons. The extracellular solution was as for LTP experiments. Pipette solution contained 140 mM KCl, 1 mM $CaCl_2$, 10 mM EGTA, 2 mM $MgCl_2$, 4 mM Na_3ATP, 0.5 mM Na_3GTP, 10 mM HEPES, pH 7.3. Spontaneous inhibitory PSCs were recorded at a holding potential of -70 mV in the presence of 10 µM CNQX and 40 µM AP5. Spontaneous excitatory PSCs were recorded at a holding potential of -70 mV in the presence of 5 µM strychnine and 5 µM bicuculline. For mIPSCs and mEPSCs recordings, 0.5 µM TTX was added to the bath solution. Signals with amplitudes of at least two times above the background noise were selected. Patches with a serial resistance of >10 MΩ, a membrane resistance of <0.2 GΩ, or leak currents of >200 pA were excluded. Data acquisition and analysis were done using commercially available software: pClamp 10.0 (Molecular Devices, Sunnyvale, CA), MiniAnalysis (SynaptoSoft, Decatur, GA) and Prism 4 (GraphPad, San Diego, CA). Statistical significance was evaluated using two-tailed unpaired Student's t-test, with or without Welch's correction or non-parametric Mann–Whitney tests, depending on the distribution of the data. Significance level was set to $P<0.05$. Numerical values are represented as mean±standard error. Data are presented as plots of cumulative probability.

***In vivo* stimulated emission depletion (STED) nanoscopy**: STED nanoscopy was performed as acute experiments; mice were sacrificed after imaging by an overdose of anesthetics. General anesthesia was initiated by pentobarbital injection (60-80 mg/kg body weight; i.p) and continued by infusion of ethohexital (40-60 mg/kg body weight and hour; i.v). To avoid movements by active respiration, mice were paralyzed with pancuronium (800 µg/kg body weight and hour, i.p.) and artificially ventilated at 100-120 stokes/min and 100-140 µl/stroke after insertion of a tracheal tube **(Berning et al., 2012).** A pedestal to fix the head was glued to the scull above the olfactory bulb, while the coverslip was glued on a circular hole upon the visual cortex. Body temperature was kept constant (36°C-38°C) throughout the experiment. For technical details regarding STED imaging see supplementary material in **(Berning et al.,**

2012). Image processing was performed using ImageJ or Fiji. For quantification of dendrites and spines, the “Simple Neurite Tracer” macro (Fiji) was used.

***In vivo* two-Photon laser scanning microscopy (2P-LSM):** Acute 2 photon imaging was performed under general anesthesia using a gas mixture of O_2:N_2O (1:1) loaded with 5% isoflurane in a closed box (flow rate: 1000 ml/min). Following initial sedation, anesthesia was applied by a mask on a heated plate and reduced flow rate (N_2O: 100-200 ml/min; O_2: 200-300 ml/min; 1.5-2% isoflurane). The respiration rate was kept below 2 per second by adjusting the isoflurane dosage and the body temperature was kept constant (36°C-38°C) throughout the experiment **(Agarwal et al., 2011)**. During imaging the skull was attached to a custom-made ring by dental cement to reduce movements. A cranial window through the parietal bone was produced inside the ring close to the sagittal suture. The exposed cortex was covered by a glass coverslip. The structural imaging was carried out by a custom-made microscope equipped with a fs-pulsed titanium-sapphire laser (Chameleon Vision II; Coherent, Glasgow, UK) and a long-distance W Plan-Apochromat 20x/1.0 water immersion objective (Zeiss; Jena, Germany). For excitation, the laser was set at 925±5 nm, and fluorescent signal was collected by a photo-multiplier tube (Hamamatsu, Japan) through a 510±42 nm band pass filter (Semrock). Uniformly spaced (0.8-2 µm) planes of 125x125 to 500x500 μm^2 regions of the cerebral cortex were recorded and processed to obtain z-stacks of images (512x512 or 1024x1024 pixels in size). Image processing was performed using Matlab (version 7, MathWorks, Ismaning, Germany) and ImageJ or Fiji.

Behavioral testings:

Open field: Spontaneous activity of *CK-Cre*Nrg1$^{f/f}$*, *CK-Cre*Nrg1$^{f/+}$ and Nrg1$^{f/+}$* mice was tested in a grey Perspex arena (120 cm in diameter, 25 cm high). Mice were placed in the center and allowed to explore for 7 min. Behavior was recorded by a PC-linked overhead video camera. Viewer software was used to calculate distance traveled and time spent in the central, intermediate or peripheral zones of the open

field. Locomotor activity and anxiety of *HA-Nrg1-tg* (males n=16, females n=10) and WT mice (males n=18, females n=18) were assessed in an open-field test using a Plexiglas box (45 x 45 x 55 cm). Mice were placed individually and allowed to explore for 10 min. Infrared sensors monitored the time spent in distinct areas of the arena (center, 70% of total area; periphery, 30%), distance travelled and rearings. Data were analyzed using ActiMot software (TSE, Bad Homburg, Germany).

Cued and contextual fear conditioning: Fear conditioning was performed as described **(Radyushkin et al., 2005)**. Briefly, mice were trained within the same session for both contextual and cued fear conditioning. Training consisted of exposing mice for 120 s to the context to assess baseline activity. This period was followed by a 10 s, 5 kHz, 85 dB tone (conditioned stimulus, CS). Immediately after the tone, a 2 s, 0.4 mA foot shock (unconditioned stimulus, US) was applied. This CS-US pairing was repeated 13 s later. All mice remained in the conditioning chamber for an additional 23 s following the second CS–US pairing. The contextual memory test was performed 48 h after training. Mice were monitored over 2 min for freezing in the same context as used for training. The cued memory test was performed 52 h after training in a new chamber. First, mice were monitored for freezing over a 2 min pre-cue period with no tone to assess freezing in the new context. Next, a 2 min cue period followed in which the tone was presented. Duration of freezing behavior, defined as the absolute lack of movement (excluding respiratory movements), was recorded by a video camera and a PC equipped with 'Video freeze' software (MED Associates, St. Albans, Vermont, USA).

MK-801 treatment: MK-801 was dissolved in saline and injected i.p. (0.3 mg/kg; volume of injection, 0.1 ml/10 g body weight). Distance travelled in the open field was recorded as described above. Baseline activity (i.e. distance travelled) was determined over 4 min time intervals for 20 min before injection. Effect of MK-801 was measured for 120 min following injection. Again, travelled distance was determined over 4 min time intervals. MK-801 induced changes in activity were expressed for each mouse as percentage of individual baseline.

Prepulse inhibition: Mice were placed in cylindrical enclosures equipped with an ultra-sensor for movement recording located in sound-attenuating cabinets (SR-LAB^{TM}, San Diego Instruments). An experimental session included (I) a 3 min habituation to the set-up and 65 dB background white noise present continuously throughout the entire experiment and (II) a test session as described previously **(Brzozka et al., 2010)**. First, six pulse-alone trials of 120 dB intensity and 40 ms duration were applied to minimize influence of within-session habituation (data not included in PPI analysis). The startle reaction to an acoustic stimulus was recorded for 80 ms starting with the onset of the stimulus. For PPI testing, the 120 dB startle pulse of 40 ms duration was applied either alone or 100 ms after a presentation of a non-startling prepulse stimulus of 70, 75 or 80 dB intensity and 20 ms duration. Different trials (10 of each type) were applied with inter-trial intervals alternating from 8 to 22 s in a pseudorandom order. PPI was calculated as follows: prepulse inhibition (%) = 100 - [(startle amplitude after prepulse and pulse) / (startle amplitude after pulse only)×100] (for details see: **(Brzozka et al., 2010)**).

Supplemental References

Agarwal, A., Dibaj, P., Kassmann, C.M., Goebbels, S., Nave, K.A., and Schwab, M.H. (2011). In Vivo Imaging and Noninvasive Ablation of Pyramidal Neurons in Adult NEX-CreERT2 Mice. Cereb Cortex.

Berning, S., Willig, K.I., Steffens, H., Dibaj, P., and Hell, S.W. (2012). Nanoscopy in a living mouse brain. Science (New York, NY 335, 551.

Brzozka, M.M., Radyushkin, K., Wichert, S.P., Ehrenreich, H., and Rossner, M.J. (2010). Cognitive and sensorimotor gating impairments in transgenic mice overexpressing the schizophrenia susceptibility gene Tcf4 in the brain. Biological psychiatry 68, 33-40.

Chen, Y.J., Johnson, M.A., Lieberman, M.D., Goodchild, R.E., Schobel, S., Lewandowski, N., Rosoklija, G., Liu, R.C., Gingrich, J.A., Small, S.*, et al.* (2008). Type III neuregulin-1 is required for normal sensorimotor gating, memory-related behaviors, and corticostriatal circuit components. J Neurosci 28, 6872-6883.

Deakin, I.H., Nissen, W., Law, A.J., Lane, T., Kanso, R., Schwab, M.H., Nave, K.A., Lamsa, K.P., Paulsen, O., Bannerman, D.M., and Harrison, P.J. (2011). Transgenic Overexpression of the Type I Isoform of Neuregulin 1 Affects Working Memory and Hippocampal Oscillations but not Long-term Potentiation. Cereb Cortex.

Dodd, P.R., Hardy, J.A., Oakley, A.E., Edwardson, J.A., Perry, E.K., and Delaunoy, J.P. (1981). A rapid method for preparing synaptosomes: comparison, with alternative procedures. Brain research 226, 107-118.

Gerlai, R., Pisacane, P., and Erickson, S. (2000). Heregulin, but not ErbB2 or ErbB3, heterozygous mutant mice exhibit hyperactivity in multiple behavioral tasks. Behavioural brain research 109, 219-227.

Jiang, L., Emmetsberger, J., Talmage, D.A., and Role, L.W. (2013). Type III neuregulin 1 is required for multiple forms of excitatory synaptic plasticity of mouse cortico-amygdala circuits. J Neurosci 33, 9655-9666.

Luo, X., He, W., Hu, X., and Yan, R. (2013). Reversible Overexpression of Bace1-Cleaved Neuregulin-1 N-Terminal Fragment Induces Schizophrenia-Like Phenotypes in Mice. Biological psychiatry.

Mizoguchi, A., Ueda, T., Ikeda, K., Shiku, H., Mizoguti, H., and Takai, Y. (1989). Localization and subcellular distribution of cellular ras gene products in rat brain. Brain Res Mol Brain Res 5, 31-44.

O'Tuathaigh, C.M., Harte, M., O'Leary, C., O'Sullivan, G.J., Blau, C., Lai, D., Harvey, R.P., Tighe, O., Fagan, A.J., Kerskens, C.*, et al.* (2010). Schizophrenia-related endophenotypes in heterozygous neuregulin-1 'knockout' mice. The European journal of neuroscience 31, 349-358.

Radyushkin, K., Anokhin, K., Meyer, B.I., Jiang, Q., Alvarez-Bolado, G., and Gruss, P. (2005). Genetic ablation of the mammillary bodies in the Foxb1 mutant mouse leads to selective deficit of spatial working memory. The European journal of neuroscience 21, 219-229.

Rimer, M., Barrett, D.W., Maldonado, M.A., Vock, V.M., and Gonzalez-Lima, F. (2005). Neuregulin-1 immunoglobulin-like domain mutant mice: clozapine sensitivity and impaired latent inhibition. Neuroreport 16, 271-275.

Rao, S., Zhou, M., Merker, R., Mann, M., Fischbach, G., and Gingrich, J. (2004). Behavioral alterations in mice with a reduced neuregulin-1 ig domain isoform. In 7th Annual Meeting; International Society for Developmental Psychobiology.

Shamir, A., Kwon, O.B., Karavanova, I., Vullhorst, D., Leiva-Salcedo, E., Janssen, M.J., and Buonanno, A. (2012). The importance of the NRG-1/ErbB4 pathway for synaptic plasticity and behaviors associated with psychiatric disorders. J Neurosci 32, 2988-2997.

Stefansson, H., Sigurdsson, E., Steinthorsdottir, V., Bjornsdottir, S., Sigmundsson, T., Ghosh, S., Brynjolfsson, J., Gunnarsdottir, S., Ivarsson, O., Chou, T.T.*, et al.* (2002). Neuregulin 1 and susceptibility to schizophrenia. Am J Hum Genet 71, 877-892.

Yin, D.M., Chen, Y.J., Lu, Y.S., Bean, J.C., Sathyamurthy, A., Shen, C., Liu, X., Lin, T.W., Smith, C.A., Xiong, W.C., and Mei, L. (2013). Reversal of behavioral deficits and synaptic dysfunction in mice overexpressing neuregulin 1. Neuron 78, 644-657.